RESEARCH ARTICLE

Surface-driven amplification of Madden–Julian oscillation circulation anomalies across East Africa and its influence on the Turkana jet

Joshua Talib[1] | Christopher M. Taylor[1,2] | Bethan L. Harris[1,2] |
Caroline M. Wainwright[3]

[1]Hydro-Climate Risks, UK Centre for Ecology and Hydrology, Wallingford, UK

[2]National Centre for Earth Observation, Wallingford, UK

[3]Grantham Institute, Imperial College London, London, UK

Correspondence
Joshua Talib, UK Centre for Ecology and Hydrology, Wallingford, OX10 8BB, UK.
Email: jostal@ceh.ac.uk

Abstract

In semi-arid environments, rainfall-driven soil moisture fluctuations exert a strong influence on surface turbulent fluxes. Intraseasonal rainfall variability can therefore impact low-level atmospheric temperatures and influence regional circulations. Using satellite observations and an atmospheric reanalysis, we investigate whether rainfall variability induced by the Madden–Julian oscillation (MJO) triggers land–atmosphere feedbacks across East Africa.

We identify that surface fluxes during the East African wet seasons (March–May and October–December) are sensitive to MJO-induced precipitation variations across low-lying regions of South Sudan and highland regions of Uganda and southwest Kenya. For example, during MJO phases 6 to 8, when rainfall is suppressed, surface temperatures and sensible heat fluxes increase, whilst evapotranspiration decreases. Spatial variations in the surface flux response to rainfall variability feed back onto the atmosphere through amplifying MJO-associated pressure anomalies. During dry MJO events for instance, surface warming across the exit region of the Turkana channel increases the low-tropospheric along-channel pressure gradient and intensifies the Turkana jet. We conclude that average surface-driven temperature fluctuations during a single day are responsible for approximately 12% of MJO-associated variability of the Turkana jet speed. However, we expect that the accumulation of heat over multiple days to the west of the East African Highlands further amplifies anomalies in the pressure gradient and jet intensity. Modelling experiments are required to quantify the accumulated impact of the surface forcing. Surface-driven Turkana jet variations influence the East African moisture budget and affect the intensity and inland propagation of coastal convection. Not only is this the first study to investigate the importance of intraseasonal land–atmosphere feedbacks across East Africa, but it is also the first to show that Turkana jet characteristics are partly driven by surface conditions. This work motivates an investigation into whether subseasonal forecast models fully harness the predictability from surface-induced jet variations.

KEYWORDS

convection, East Africa, intraseasonal variability, land surface, soil moisture–atmosphere feedbacks

1 | INTRODUCTION

In arid and semi-arid regions, variations in surface soil moisture influence the partitioning of surface turbulent fluxes and affect characteristics of land–atmosphere coupling. For example, when a semi-arid surface dries and sensible heat is favoured over latent heat (Teuling *et al.*, 2006; Miralles *et al.*, 2012; Gallego-Elvira *et al.*, 2016), near-surface air temperatures can increase and the planetary boundary layer may deepen (Koster *et al.*, 2009; Miralles *et al.*, 2012; Berg *et al.*, 2014; Schwingshackl *et al.*, 2017). This control of surface soil moisture on turbulent fluxes and planetary boundary-layer conditions is a source of short-term (days) predictability for characteristics of mesoscale daytime circulations (Pielke Sr., 2001; Taylor *et al.*, 2007; Taylor, 2015) and deep convection (Taylor *et al.*, 2012; Bhowmick and Parker, 2018; Klein and Taylor, 2020; Barton *et al.*, 2021). Focusing on intraseasonal time-scales, modelling experiments have shown that improving the initialisation of soil moisture increases subseasonal forecast skill for temperature and, to a lesser extent, precipitation (Koster *et al.*, 2011; van den Hurk *et al.*, 2012; Dirmeyer *et al.*, 2018). A substantial amount of this work has focused on the predictability during boreal summer across midlatitude continental regions. There has been somewhat less attention devoted to tropical regions, where atmospheric modes of variability, notably the Madden–Julian oscillation (MJO; Madden and Julian, 1994), drive a large proportion of intraseasonal precipitation variability (Mutai and Ward, 2000; Mpeta and Jury, 2001; Pohl and Camberlin, 2006a; Pohl and Camberlin, 2006b; Berhane and Zaitchik, 2014; Finney *et al.*, 2020b) and impact surface conditions, including soil moisture (Peng *et al.*, 2017) and vegetation water content (Harris *et al.*, 2022). In this study, we explore the potential for intraseasonal land–atmosphere feedbacks in East Africa, where MJO forcing drives strong regional rainfall fluctuations on time-scales of 30 to 60 days (Pohl and Camberlin, 2006a; Berhane and Zaitchik, 2014). Given that most of East Africa is a semi-arid or arid environment, where surface turbulent fluxes are sensitive to soil moisture variations (Gallego-Elvira *et al.*, 2016; Soares *et al.*, 2019), we expect surface turbulent fluxes to be strongly modulated by the MJO, and in turn possibly feed back onto the atmosphere at similar scales to the original precipitation forcing.

Though intraseasonal rainfall variability is smaller than daily to weekly fluctuations across the majority of the Tropics (Moron and Robertson, 2021), previous studies have shown the importance of tropical intraseasonal land–atmosphere feedbacks (Saha *et al.*, 2012; Unnikrishnan *et al.*, 2017; Chug and Dominguez, 2019; Talib *et al.*, 2022). Within the Tropics, most studies have focused

on the impact of intraseasonal precipitation variability on land–atmosphere coupling across India (Sikka and Gadgil, 1980; Srinivasan *et al.*, 1993; Ferranti *et al.*, 1999; Saha *et al.*, 2012; Unnikrishnan *et al.*, 2017). For example, observations and modelling experiments have shown that the intensity of intraseasonal variations of the South Asian monsoon partly depend on surface soil moisture conditions (Sikka and Gadgil, 1980; Webster, 1983; Gadgil and Asha, 1992; Annamalai and Slingo, 2001). Meanwhile across South America, variations in vegetation impact low-level atmospheric temperatures which influence the regional circulation and precipitation accumulations (Chug and Dominguez, 2019). Studies focusing on intraseasonal land–atmosphere feedbacks across Africa have investigated processes during the West African monsoon (Taylor *et al.*, 2007; Lavender and Matthews, 2009; Talib *et al.*, 2022), as the surface flux response to rainfall variability is particularly strong across the Sahel (Guo *et al.*, 2006; Dirmeyer, 2011; Miralles *et al.*, 2012; Gallego-Elvira *et al.*, 2016). Talib *et al.* (2022) show that characteristics of 20- to 60-day variability of the West African monsoon are partly controlled by Sahelian surface soil moisture anomalies feeding back onto the regional circulation. For example, Sahelian surface drying driven by an intraseasonal dry spell increases boundary-layer temperatures and shifts the shallow meridional circulation southwards. Though it is evident from previous studies that anomalous land–atmosphere coupling can influence characteristics of tropical intraseasonal variability, an investigation into subseasonal land–atmosphere feedbacks across East Africa is yet to take place.

East Africa is topographically diverse with a variety of biomes (Figure 1) and is one of the most meteorologically complex regions on the African continent (Nicholson, 2017). In general, East Africa has two wet seasons, the March–May (MAM) long rains and the October–December (OND) short rains, which correspond to periods when the intertropical convergence zone crosses the Equator (Mutai and Ward, 2000; Camberlin and Philippon, 2002; Yang *et al.*, 2015). Many studies have shown that intraseasonal rainfall variability across East Africa is predominately driven by the MJO (Mutai and Ward, 2000; Mpeta and Jury, 2001; Pohl and Camberlin, 2006a; Pohl and Camberlin, 2006b; Berhane and Zaitchik, 2014; Finney *et al.*, 2020b). For example, enhanced precipitation across the East African Highlands occurs when the convective core of the MJO is situated over the Indian Ocean and the well-established Matsuno–Gill response (Matsuno, 1966; Gill, 1980) enhances low-level westerlies and moisture transport from the Congolese rainforest (Berhane and Zaitchik, 2014; Finney *et al.*, 2020b). The orography of East Africa, shown in Figure 1a, influences the direction and strength of the low-tropospheric wind (Kinuthia, 1992;
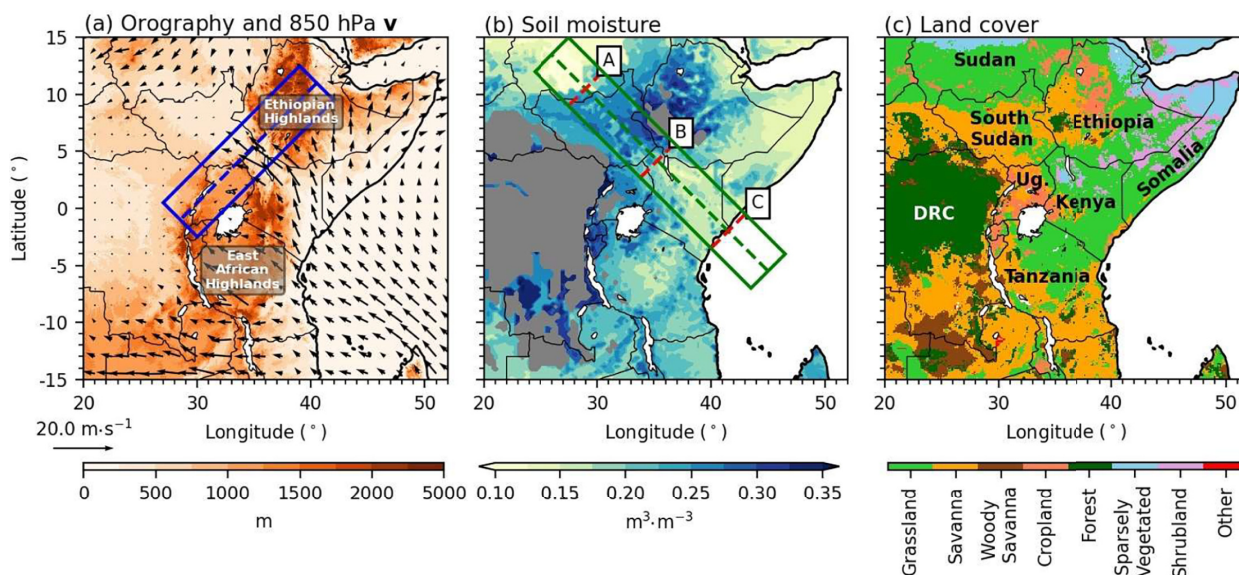
FIGURE 1 (a) Average European Centre for Medium-Range Weather Forecasts Reanalysis version 5 850 hPa 0000 UTC horizontal wind (m·s^{-1}, vectors) and orography (m, filled), (b) European Space Agency Climate Change Initiative surface soil moisture (m^3 ·m^{-3}) during East African wet seasons (March–May and October–December), and (c) moderate-resolution imaging spectroradiometer (MODIS) International Geosphere Biosphere Programme (IGBP) land cover classification. Transects perpendicular and parallel to the Turkana channel used in this study are denoted by blue and green rectangles in (a) and (b) respectively. Dashed lines in each rectangle denote the transect centre which is used for axis labels. Red dashed lines perpendicular to the Turkana channel in (b), and associated labels, highlight transect locations where there is a strong along-channel surface gradient. For panel (c) certain MODIS IGBP land cover classifications are combined to improve visualisation. "Forest" includes all forest surface classes, including evergreen broadleaf and mixed forests; "shrubland" combines both open and closed shrublands; "other" includes permanent wetlands and urban. Panels (a) and (c) also highlight mountain ranges and countries referred to in this study, with "Ug." and "DRC" being shorthand for Uganda and Democratic Republic of Congo respectively [Colour figure can be viewed at wileyonlinelibrary.com]

Indeje *et al.*, 2001) and drives spatial rainfall variations (Nicholson, 2017; Vizy and Cook, 2019; Munday *et al.*, 2021). A key feature of the East African climate that is influenced by orography and has been observed by radiosondes (Kinuthia and Asnani, 1982; Kinuthia, 1992; Munday *et al.*, 2022) is the Turkana jet, a strong south-easterly low-level jet at approximately 850 hPa between the Ethiopian Highlands and East African Highlands (Figure 1a). Modelling experiments (Indeje *et al.*, 2001) and observations of higher jet speeds across narrower parts of the channel (Kinuthia, 1992) suggest a Bernoulli forcing on jet characteristics and that the shape of the Turkana channel controls the low-level jet's orientation and direction. Meanwhile, the seasonal cycle of the jet intensity illustrates that jet characteristics are also partly controlled by the temperature gradient along the Turkana channel (Hartman, 2018; Vizy and Cook, 2019). Maximum jet speeds are observed in September, associated with the Somali jet advecting relatively cool air onto low-lying coastal regions of East Africa and increasing the along-channel temperature gradient (Hartman, 2018). As observed for other low-level jets (Helfand and Schubert, 1995; Banta *et al.*, 2002; Parker *et al.*, 2005; Du *et al.*, 2014), the Turkana jet intensity has a nocturnal maximum (Nicholson, 2016; Hartman, 2018), with two

mechanisms being proposed for this substantial diurnal cycle. The first is based on jet intensification being prohibited during the daytime due to strong daytime coupling between the boundary layer and turbulent surface fluxes. During the night meanwhile, surface turbulent fluxes minimise and the boundary-layer depth diminishes, leading to a decoupling of surface and boundary-layer processes and allowing the Turkana jet to intensify (Nicholson, 2016; Hartman, 2018). The second proposed mechanism is that enhanced nocturnal cooling at higher altitudes parallel to the jet drives katabatic winds that intensify the nocturnal acceleration of the Turkana jet (Parish and Oolman, 2010; Nicholson, 2016). As the Turkana jet partly controls water vapour transport from low-lying regions of East Africa to the interior of the African continent (Viste and Sorteberg, 2013; Munday *et al.*, 2022), it influences local precipitation rates (Nicholson, 2016; Vizy and Cook, 2019; Munday *et al.*, 2021). For example, enhanced moisture divergence at the jet entrance suppresses local convection. The influence of the Turkana jet on precipitation drives a surface aridity gradient with relatively dry and wet surface conditions across the entrance and exit regions of the jet respectively (Fig. 1b; Munday *et al.*, 2023).

Soil moisture can influence nocturnal jets, as demonstrated in the Great Plains of the USA (Campbell

et al., 2019; Ferguson *et al.*, 2020). Campbell *et al.* (2019) performed modelling experiments to understand the influence of anomalous soil moisture on the Great Plains low-level jet (Bonner, 1968) when it is uncoupled from the upper level jet stream (Burrows *et al.*, 2019). Though decreased soil moisture across the Great Plains increases daytime sensible heating and the planetary boundary-layer height, a jet intensification is prohibited until after sunset due to frictional forces imposed by strong daytime turbulent fluxes. Campbell *et al.* (2019) propose two mechanisms by which decreased soil moisture intensifies the Great Plains low-level jet. Following Blackadar (1957), the first mechanism is associated with the collapse of the planetary boundary layer at sunset, which forms an inertial oscillation that accelerates nocturnal ageostrophic winds. The second mechanism, consistent with Holton (1967), is associated with the development of a thermal low in the exit region of the low-level jet, which increases the meridional gradient in low-tropospheric geopotential height and intensifies geostrophic winds. Under both mechanisms, a drier surface leads to a more intense nocturnal low-level jet. Campbell *et al.* (2019) conclude that a dry surface leads to a stronger Great Plains jet by up to $4 \, \mathrm{m \cdot s^{-1}}$ compared with a wet surface. In light of anomalous soil moisture partly controlling the intensity of the Great Plains low-level jet, Ferguson *et al.* (2020) show that daily forecasts of the low-level jet are improved when satellite-based soil moisture observations are assimilated into forecast initialisation. Motivated by Campbell *et al.* (2019), we investigate whether MJO-induced surface turbulent flux variations across East Africa influence the Turkana jet intensity.

Given the importance of land–atmosphere feedbacks on characteristics of rainfall variability in tropical semi-arid regions (Saha *et al.*, 2012; Taylor *et al.*, 2012; Chug and Dominguez, 2019; Klein and Taylor, 2020; Talib *et al.*, 2022) and that the MJO substantially modulates precipitation across East Africa, (Mutai and Ward, 2000; Mpeta and Jury, 2001; Pohl and Camberlin, 2006a; Pohl and Camberlin, 2006b; Berhane and Zaitchik, 2014; Finney *et al.*, 2020b), this study investigates whether MJO-induced land–atmosphere feedbacks influence aspects of intraseasonal variability across East Africa. Section 2 describes the observations and atmospheric reanalysis utilised in this study. To explore the influence of land–atmosphere feedbacks on characteristics of the MJO, we first show the surface response to MJO-induced anomalous precipitation in Section 3.1. We then investigate whether surface flux perturbations feed back onto the Turkana jet and atmospheric circulation (Section 3.2), before exploring whether land–atmosphere feedbacks influence rainfall characteristics across East Africa (Section 3.3). Finally, Sections 4 and 5 close the paper with the discussion and conclusions respectively.

2 | METHODOLOGY

In this study, multiple observational products are used to understand MJO-induced land–atmosphere feedbacks across East Africa. Table 1 provides an overview of all datasets utilised. Two precipitation products are used to investigate MJO-induced rainfall variations across East Africa: the Climate Hazards Group Infrared Precipitation with Stations (CHIRPS) dataset, which combines satellite-derived infrared measurements with gauge-based rainfall totals (Funk *et al.*, 2015); and the Integrated Multi-satellite Retrievals for the Global Precipitation Measurement mission (GPM IMERG) version 6B, which utilises satellite-based passive microwave and geosynchronous infrared measurements (Huffman *et al.*, 2019). GPM IMERG is also adjusted using monthly values from the Global Precipitation Climatology Project (GPCP; Adler *et al.*, 2003). For the majority of this study we focus on daily precipitation on a 0.05° latitude–longitude grid from CHIRPS, as CHIRPS has a longer time span than GPM IMERG (Table 1). Three-hourly GPM IMERG rainfall accumulations on a 0.1° latitude–longitude grid are used to investigate sub-daily rainfall variations associated with MJO-induced land–atmosphere feedbacks.

Two satellite-derived datasets are used to analyse changes in the land-surface state. First, changes in the surface soil moisture are investigated using the European Space Agency Climate Change Initiative combined soil moisture product version 6.1 (Dorigo *et al.*, 2017; Gruber *et al.*, 2017; Gruber *et al.*, 2019; van der Schalie *et al.*, 2021). This combined soil moisture product utilises four active and ten passive microwave-based instruments. It also uses a global land data assimilation system (GLDAS; Rodell *et al.*, 2004) to obtain a consistent climatology (Gruber *et al.*, 2019). There is no common definition for the surface soil moisture depth examined by microwave-based instruments (Dorigo *et al.*, 2017); however, it is generally assumed to be in the range of 2 to 5 cm (Ulaby, 1982). Second, we analyse vegetation optical depth (VOD) observations from the Vegetation Optical Depth Climate Archive dataset (Moesinger *et al.*, 2020), as MJO-driven vegetation changes may cause more persistent turbulent flux anomalies than those associated with surface soil moisture variations. VOD, derived from satellite-based microwave radiation measurements, is a proxy for vegetation water content and responds to changes in water stress and aboveground biomass (Meesters *et al.*, 2005; Momen *et al.*, 2017; van der Schalie *et al.*, 2017; Konings *et al.*, 2021). Rodríguez-Fernández *et al.* (2018) show that VOD is a good indicator for vegetation biomass across Africa. In this study, we use VOD observations retrieved between 2000 and 2018 in the X-band ($\approx$10.7 GHz), and apply the same quality control procedure as Talib *et al.* (2022) to

TABLE 1 Details of observational and reanalysis products used in this study.

Variable	Data source	Time span	Resolution		Reference
			Spatial	Temporal	
Precipitation	CHIRPS	1981–2020	0.05°	Daily	Funk et al. (2015)
Precipitation	GPM IMERG	2000–2020	0.1°	Three-hourly	Huffman et al. (2019)
Surface soil moisture	ESA CCI	1981–2020	0.25°	Daily	Dorigo et al. (2017)
Vegetation optical depth	VODCA	2000–2018	0.25°	Daily	Moesinger et al. (2020)
Land surface temperature	MODIS	2000–2020	1 km[a]	Daily	Sobrino and Romaguera (2004)
Surface radiative fluxes	CERES	2000–2020	1.0°	Daily	Loeb et al. (2003)
Evapotranspiration	GLEAM3.2, ERA5, GLDAS2, MERRA2, and flux tower measurements	1981–2017	0.25°	Daily	Lu et al. (2021)
Land cover type	MODIS IGBP	2020	0.1°	Annual	Friedl and Sulla-Menashe (2015)
Atmospheric conditions, including temperature, wind, geopotential, and humidity	ERA5	1981–2020	1.5°	Three-hourly	Hersbach et al. (2019)

[a] Averaged to 0.1° latitude-longitude grid.

Abbreviations: CERES, clouds and earth's radiant energy system; CHIRPS, climate hazards group infrared precipitation with stations; ERA5, European centre for medium-range weather forecasts reanalysis version 5; ESA CCI, European space agency climate change initiative; GLDAS2, global land data assimilation system version 2; GLEAM3.2, global land evaporation Amsterdam model version 3.2a; IGBP, international geosphere biosphere programme; IMERG, integrated multi-satellite retrievals for global precipitation measurement (GPM); MERRA2, modern-era retrospective analysis for research and applications version 2; MODIS, moderate-resolution imaging spectroradiometer; VODCA, vegetation optical depth climate archive.

remove spurious observations and VOD fluctuations that are caused by inundation.

To identify changes in the surface energy balance associated with MJO-induced soil moisture variations, we use clear-sky daytime land-surface temperature (LST) measurements from the moderate-resolution imaging spectroradiometer (MODIS) instruments on the Terra and Aqua satellites (Wan and Hook, 2015). Anomalous clear-sky LST is used as a proxy for the partitioning between surface sensible and latent heat fluxes, as in semi-arid regions LST fluctuations drive boundary-layer temperatures rather than vice versa. Under this assumption, positive clear-sky LST anomalies indicate increased sensible heating, whereas negative LSTs depict enhanced latent heat fluxes. Thermal infrared measurements from Terra and Aqua satellites are available from respectively 2000 and 2002 onwards, with daytime equatorial crossing times of approximately 1030 and 1330 local time respectively. In this study we use LSTs at a 1 km resolution from the MOD11A1 version 6 product, which derives pixel temperatures from the MOD11L2 swath product. Using a similar technique to Folwell et al. (2016) and Gallego-Elvira et al. (2016), we only retain observations with view angles of less than ±40° and that are flagged as cloud and aerosol free. We do, however, include observations with an emissivity error ≤0.02, as using the strictest threshold of 0.01 dramatically reduces the number of valid measurements across dry regions of north and central Kenya (not shown). Following Trigo et al. (2008), on days when a valid observation exists from both Terra and Aqua satellites, only the observed temperature from the lowest viewing angle is used. In this work we analyse daily LST anomalies relative to a monthly climatology, as using anomalous values reduces spatial sampling errors caused by partially cloud-free regions and allows us to combine data from both satellites. Anomalies are computed on a 1 km grid for Aqua and Terra measurements separately. Using these anomalies, we then calculate the average LST anomaly at a 0.1° latitude–longitude resolution. We only analyse measurements at a 0.1° resolution if there are at least 20 pixels with a valid observation within the gridbox (≈20% or more of the gridbox area).

Although analysing MODIS LSTs supports our understanding of MJO-induced changes in the surface energy balance, it only highlights fluctuations in the partitioning between surface sensible and latent heat fluxes under clear-sky conditions. In light of this, we also analyse all-sky surface flux anomalies. To investigate changes in surface radiation, hourly mean fluxes are extracted from the Clouds and Earth's Radiant Energy

System (CERES; Loeb *et al.*, 2003), which are derived through combining (Kato *et al.*, 2018) observed filtered top-of-the-atmosphere short-wave and long-wave irradiance (Loeb *et al.*, 2003), cloud properties retrieved by MODIS and geostationary satellites (Minnis *et al.*, 2011), and temperature, specific humidity, and ozone profiles from the Goddard Earth Observing System version 5.4.1 reanalysis (Rienecker *et al.*, 2008). Observational estimates of daily evapotranspiration (ET) are inherently uncertain as they rely on parametrisations to link relatively well-observed variables (e.g., LST, soil moisture, VOD, and atmospheric humidity deficit) to the land–atmosphere flux. To provide supporting evidence for our interpretation of the MJO-induced surface flux response inferred from LST, we use a harmonised land ET dataset on a 0.25° latitude–longitude grid (Lu *et al.*, 2021). This ET dataset combines three model-based products: the European Centre for Medium-Range Weather Forecasts (ECWMF) Reanalysis version 5 (ERA5; Copernicus Climate Change Service (C3S), 2017; Hersbach *et al.*, 2020), the Global Land Data Assimilation System version 2 (GLDAS2; Rodell *et al.*, 2004), and the Modern-Era Retrospective Analysis for Research and Applications version 2 (MERRA2; Gelaro *et al.*, 2017). These three products are combined using a reliability ensemble averaging method (Giorgi and Mearns, 2002), with flux tower observations and the Global Land Evaporation Amsterdam Model version 3.2a (GLEAM3.2a; Miralles *et al.*, 2011) used for reference and evaluation (Lu *et al.*, 2021). It should be noted that only one flux tower used for reference by Lu *et al.* (2021) is located in East Africa, situated in southern Sudan, whereas eight flux towers are located in savanna environments.

To investigate the atmospheric response to MJO-induced surface changes, we use ERA5 (Copernicus Climate Change Service (C3S), 2017; Hersbach *et al.*, 2020). We analyse data from 1979 to 2020 at three-hourly intervals, on a 1.5° latitude–longitude grid across 22 pressure levels (1000 to 50 hPa in increments of 50 hPa with the addition of 975 and 925 hPa). ERA5, computed using four-dimensional variational data assimilation and cycle 41r2 of the Integrated Forecasting System, provides a detailed record of the global atmosphere, land, and ocean waves (Hersbach *et al.*, 2018; Hersbach *et al.*, 2019). ERA5 surface conditions are formulated using the Hydrology-Tiled ECMWF Scheme for Surface Exchanges over Land land-surface model (Balsamo *et al.*, 2015), which is forced using assimilated near-surface meteorological observations and soil moisture data from the Advanced Scatterometer (ASCAT; Wagner *et al.*, 2013; ECMWF, 2016). The use of Advanced Scatterometer observations to assimilate soil moisture improves the representation of planetary boundary-layer

dynamics (Aires *et al.*, 2021). To minimise the impact of sampling across different months, we analyse all variables using anomalies relative to a monthly climatology and, where applicable, relative to hourly climatologies of the respective month.

To investigate MJO-induced land–atmosphere feedbacks, we downloaded MJO indices provided by the Australian Government Bureau of Meteorology (Wheeler and Hendon, 2004). These MJO indices are computed using zonal winds at 850 and 200 hPa from the reanalysis product produced by the National Centers for Environmental Prediction and the National Center for Atmospheric Research (NCAR; Kalnay *et al.*, 1996), and daily-mean outgoing long-wave radiation satellite observations (Liebmann and Smith, 1996) from the National Oceanic and Atmospheric Administration. The two leading empirical orthogonal functions associated with these variables, and the corresponding principal components (PC1 and PC2), are used to diagnose the phase and amplitude of the MJO (Wheeler and Hendon, 2004). In this study, the same phase definitions as Wheeler and Hendon (2004) are used. For example, stronger convection across the Maritime Continent is defined as either MJO phase 4 or 5. We also assume that the MJO is inactive when the square root of the sum of the squared principal component indices is smaller than one. To simplify our analysis of MJO-induced land–atmosphere feedbacks, we focus on feedbacks during both wet seasons across East Africa, the MAM long rains and the OND short rains, and treat all anomalies in all months equally. Whilst for the majority of this study we refer to the time of day in reference to coordinated universal time (UTC), we also refer to the local time zone, East Africa Time (EAT). EAT is 3 hr ahead of UTC. Unless stated, statistical significance is defined when the *P*-value of an independent *t*-test is smaller than 0.05.

3 | RESULTS

3.1 | Surface response to MJO-induced precipitation variability

Given that MJO-induced rainfall anomalies are significant across East Africa (Pohl and Camberlin, 2006a; Berhane *et al.*, 2015) and that a particular MJO phase typically persists for between 5 and 10 days (Madden and Julian, 1994), a surface flux response to MJO-induced rainfall variability is expected. To investigate this response, we composite all days in MJO phases 6–8 and 2–4, as during these phases East African rainfall is typically suppressed and enhanced respectively (Pohl and Camberlin, 2006a; Berhane *et al.*, 2015). In this study, we refer to days in MJO phases 6–8 and 2–4 as "dry" and
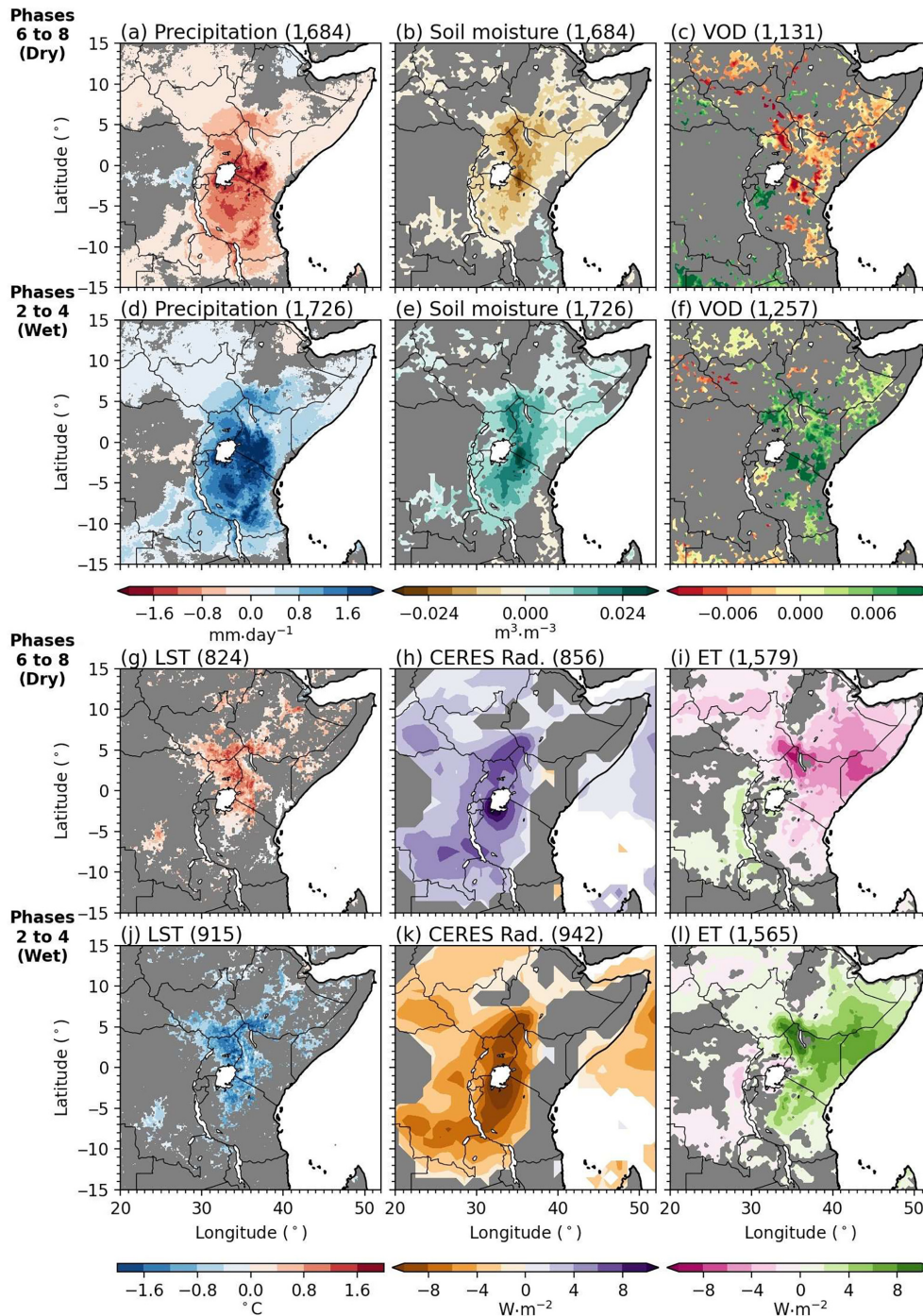
FIGURE 2 Average anomalies relative to the monthly climatology in (a, d) Climate Hazards Group Infrared Precipitation with Stations daily-accumulated precipitation (mm·day^{-1}), (b, e) surface soil moisture (m^3·m^{-3}), (c, f) vegetation optical depth (VOD; dimensionless), (g, j) land-surface temperature (LST; °C), (h, k) the surface net downward short-wave radiation combined with downward long-wave radiation (W·m^{-2}), and (i, l) evapotranspiration (ET; W·m^{-2}) during days when the Madden–Julian oscillation (MJO) is in phases (a–c, g–i) 6 to 8 and (d–f, j–l) 2 to 4. VOD anomalies are an average of measurements taken at a 15- to 20-day lag from active MJO days. Anomalies are only shown if the differences between the dry and wet MJO days are significant at a 95% confidence level according to a two-tailed t-test; grey shading denotes insignificant regions. White shading on land regions in (g) and (j) denotes areas with less than 50 valid LST observations. The number of days in each subset is presented in the title of each panel. [Colour figure can be viewed at wileyonlinelibrary.com]

"wet" MJO days respectively, regardless of daily precipitation totals. Figure 2a,d shows the average anomalous CHIRPS daily precipitation total during dry and wet MJO days. Anomalies are only shown if the difference between dry and wet MJO days is significant at a 95% confidence level according to a two-tailed t-test. Consistent with previous studies (Pohl and Camberlin, 2006a; Berhane *et al.*, 2015), MJO-induced precipitation anomalies are significant across inland regions of Kenya, Tanzania, Uganda, and South Sudan. We also observe significant precipitation differences across relatively dry regions, including Somalia, northern Kenya, and southern Ethiopia.

Focusing on the anomalous land-surface state induced by dry and wet MJO days, averaged anomalous surface soil moisture highlights a surface response to MJO-induced precipitation variability (Figure 2b,e). During dry MJO days, significant surface drying is observed across parts of the East African Highlands and low-lying regions in Kenya, northern Tanzania, northeastern Uganda, and southeastern South Sudan (Figure 2b). We also observe significant surface drying, albeit to a smaller degree, across

shrubland areas, including parts of northern Kenya, Somalia, and Ethiopia. During wet MJO days meanwhile, surface moistening is observed (Figure 2e). As expected, and consistent with Peng *et al.* (2017), the surface soil moisture response is associated with MJO-induced anomalous precipitation, as changes in surface soil moisture are driven by precipitation totals. There are some areas in East Africa (e.g., southern Tanzania, northern South Sudan, and southeast Kenya) where significant precipitation anomalies are observed (Figure 2a,d), but they do not produce significant soil moisture differences (Figure 2b,e). Such behaviour is to be expected given the differences in quality of soil moisture retrievals across such a diverse landscape. We also expect surface soil moisture in relatively dry areas to be more strongly driven by daily variability in antecedent rainfall. Alongside investigating the surface soil moisture response to MJO-induced precipitation variations, we also analyse VOD anomalies. Harris *et al.* (2022) show that vegetation in East Africa responds to intraseasonal (40- to 60-day) precipitation variability with a lag of approximately 15–20 days (Supporting Information Figure S1). We therefore present VOD anomalies averaged 15–20 days after dry and wet MJO days (Figure 2c,f). In general, dry MJO days lead to reduced VOD across grasslands in Kenya, southern South Sudan, and Tanzania (Figure 2c), whereas wet MJO days enhance subsequent VOD (Figure 2f). This VOD response is expected, as increased surface water promotes vegetation growth. The observed VOD response suggests that though instantaneous surface changes may improve atmospheric predictability during the MJO event itself, the delayed vegetation response may improve predictability at a longer lead time.

To begin investigating whether the surface response to MJO-induced anomalous precipitation (Figure 2a–f) feeds back onto the atmosphere, we first aim to understand whether anomalous surface soil moisture (Figure 2b,e) leads to fluctuations in the surface energy balance. Figure 2g,l shows average anomalies in clear-sky LST, net downward short-wave radiation combined with downward long-wave radiation, and ET. Clear-sky LST anomalies provide a proxy for the partitioning between surface sensible and latent heat fluxes, with positive LST anomalies indicating enhanced sensible heat fluxes. We find significant LST differences between dry and wet MJO days in locations with a strong soil moisture response, notably across parts of Uganda, southern South Sudan, Kenya, and northwestern Tanzania (Figure 2g,j). Enhanced LSTs during dry MJO days is consistent with evaporation being controlled by surface soil moisture rather than available energy. The lack of significant LST differences in areas with a weaker soil moisture response is in part due to fewer LST observations (the LST record is approximately half the

length of precipitation and soil moisture; Table 1) and, in places, persistent cloud cover.

So far we have identified areas where surface soil moisture anomalies are strong enough to drive consistent changes in the partitioning of surface turbulent fluxes between sensible and latent heating. However, the MJO is also expected to affect the total available energy at the surface via changes in cloud cover and downwelling radiative fluxes. To examine this effect, Figure 2h,k show the anomalies in radiative forcing, expressed here as the sum of surface net downward short-wave and downward long-wave radiation anomalies, during dry and wet MJO days respectively. During dry MJO days, positive anomalies in daily radiative fluxes are extensive and reach up to $10\,\text{W}\cdot\text{m}^{-2}$ across the East African Highlands, Uganda, and southern South Sudan (Figure 2h). This radiative effect will enhance both sensible and latent heat fluxes across the region. Considering the impacts of both changes in radiative fluxes and the partitioning of turbulent heat fluxes, we expect widespread regional atmospheric warming, via enhanced radiative fluxes, plus more localised enhancements, due to limited soil moisture, in a hotspot area covering parts of Uganda, South Sudan, and western Kenya. We find strong support for this process from the composite of ET (Figure 2i,l). Within the hotspot, ET is reduced by 4–$8\,\text{W}\cdot\text{m}^{-2}$ during dry MJO days in spite of enhanced radiative fluxes. Towards southern and eastern edges of the Congolese rainforest on the other hand, a climatological wetter surface (Figure 1b) reduces the limitation induced by drier soils, and ET increases during dry MJO days in response to enhanced radiation. Note that similar changes in radiative and turbulent fluxes are observed when using ERA5-land (Muñoz Sabater, 2019) and when only analysing MJO days that occur in the common time span (2000 to 2017) of all satellite products (not shown).

To investigate the lagged surface energy balance response to MJO-induced vegetation changes (Figure 2c,f), we compute average anomalies in components of the surface energy balance at a 15- to 20-day lag from dry and wet MJO days (Supporting Information Figure S2). Though the lagged vegetation response suggests there is potential for the surface to feed back onto the atmosphere after the MJO event itself, we do not observe a significant surface energy balance response co-located with vegetation changes (Supporting Information Figure S2). As we do not observe a significant lagged surface energy balance response to the MJO, we focus on land–atmosphere feedbacks during wet and dry MJO days, as this is when we expect a coherent atmospheric response to be maximised.

Through using several satellite products we have shown that the surface responds to MJO-induced precipitation variations. Not only does anomalous precipitation

impact the amount of surface soil moisture across East Africa, but it also changes the partitioning of the surface energy balance and affects subsequent vegetation growth. Previous studies focusing on West Africa have shown that anomalous LSTs driven by precipitation variability can feed back onto the atmosphere (Taylor *et al.*, 2007; Talib *et al.*, 2022). Using this as motivation, in the following subsection we investigate whether the observed instantaneous surface response to MJO-induced anomalous precipitation feeds back onto atmospheric conditions across East Africa.

3.2 | Atmospheric response to MJO-induced surface changes

MJO-induced precipitation variations across East Africa lead to significant changes in surface characteristics and components of the surface energy balance (Section 3.1). To investigate whether the atmosphere responds to MJO-induced perturbations in surface heating, Figure 3 shows the average anomalous near-surface air temperature, surface pressure, and 850 hPa horizontal wind during dry and wet MJO days at 1500 and 0300 UTC (1800 and 0600 EAT respectively). We also show the difference between anomalies at 1500 and 0300 UTC. Though significant daytime near-surface temperature anomalies are observed across the majority of inland regions west of 38° longitude (Figure 3a,d), presumably associated with anomalous surface radiation (Figure 2h,k), the largest temperature perturbations are observed where soil moisture and LST anomalies are strongest (Figure 2b,e,g,j). For example, Figure 3a shows daytime near-surface temperature anomalies of at least 0.6°C across southern South Sudan, western Kenya, and northern Uganda during dry MJO days. Not only does the co-location of the strongest anomalous surface and atmospheric temperatures indicate a surface forcing, but the difference between temperature anomalies at 1500 and 0300 UTC provides further evidence of a surface–atmosphere interaction (Figure 3c,f). Near-surface temperature anomalies are larger at 1500 UTC compared with 0300 UTC, as turbulent surface fluxes and heat accumulated in the planetary boundary layer peak at approximately midday and during the afternoon respectively. After sunset meanwhile, surface-induced near-surface temperature anomalies begin to dissipate as turbulent surface fluxes reduce close to zero.

As well as near-surface temperature anomalies, we also observe significant differences in anomalous horizontal wind and surface pressure between dry and wet MJO days (Figure 3g–l). As illustrated in Pohl and Camberlin (2006a) and Berhane *et al.* (2015), dry and wet MJO days are associated with anomalous easterlies and

westerlies respectively across East Africa. These wind anomalies are particularly large in the Turkana channel and are consistent with large-scale surface pressure anomalies. For example, anomalous easterlies prevail during dry MJO days associated with negative and positive pressure anomalies to the west and east of the East African Highlands respectively (Figure 3g,h). Across the exit region of the Turkana jet, where LST and daytime near-surface temperature anomalies are large (Figures 2g,j and 3a,d), there is a strong diurnal variation in surface pressure (Figure 3i,l). For instance, during dry MJO days, differences in surface pressure anomalies between 1500 and 0300 UTC maximise at approximately 0.15 hPa (Figure 3i). This is consistent with a hydrostatic response to anomalous daytime warming of approximately 0.4°C (Figure 3c) and a boundary-layer depth of approximately 1,500 m (later shown in Figure 4). Though temperature and pressure anomalies maximise during the daytime due to strong turbulent fluxes, wind anomalies maximise during nocturnal hours. For example, the largest anomalies, in absolute terms, occur in the Turkana channel and reach approximately 2.0 m·s^{-1} at night (Figure 3h,k). Larger wind anomalies during the night-time re-emphasise a surface–atmosphere interaction, as strong daytime turbulent fluxes and boundary-layer turbulence prohibit a low-level wind response to anomalous surface conditions during the daytime. The low-level wind only responds once turbulent fluxes begin to dissipate during the evening, leading to a nocturnal wind maximum. As the largest diurnal variations in anomalous horizontal wind are observed across the Turkana channel, we focus on understanding the influence of MJO-induced surface anomalies on the Turkana jet.

We have already observed during dry MJO days that enhanced sensible heating strongly warms the boundary layer on the continental side of the Turkana channel. This heat anomaly increases the existing pressure gradient, which leads to an intensification of the Turkana jet. To investigate this potential link between surface warming and the Turkana jet, Figure 4 shows vertical cross-sections perpendicular to the Turkana channel of average anomalous temperature, geopotential height, channel-orientated wind speed, and specific humidity during dry MJO days at 1500 and 0300 UTC. The cross-sections are centred at the exit region of the Turkana channel (Figure 1a) where daytime near-surface temperature anomalies are strong (Figure 3a,d). The channel-orientated wind speed is calculated at a bearing of 315° using both horizontal wind components. We also show climatological values for the seasons sampled (MAM and OND). Positive temperature anomalies in the hotspot region are maximised below 800 hPa at 1500 UTC, and weaken overnight (Figure 4a). This is consistent with a localised warming of the planetary

FIGURE 3 Average anomalies relative to the monthly climatology in (a–f) near-surface air temperature (°C, filled), (g–l) surface pressure (hPa, filled), and (a–l) 850 hPa horizontal wind (m·s⁻¹, vectors) during days in Madden–Julian oscillation (MJO) phases (a–c, g–i) 6 to 8 and (d–f, j–l) 2 to 4 at (first column) 1500 UTC and (second column) 0300 UTC. Panels in third column show the difference in anomalies at 1500 and 0300 UTC. Anomalies are only shown if the differences between dry and wet MJO days are significant at the 95% confidence level; grey shading denotes insignificant regions. Wind vectors are displayed if significantly different in either a meridional or zonal direction. We also remove wind vectors if the surface pressure is lower than 850 hPa during any point of the time series (i.e., across the Ethiopian Highlands). The orange rectangles in panels (i) and (l) highlight the area used for the exit region of the Turkana channel. [Colour figure can be viewed at wileyonlinelibrary.com]
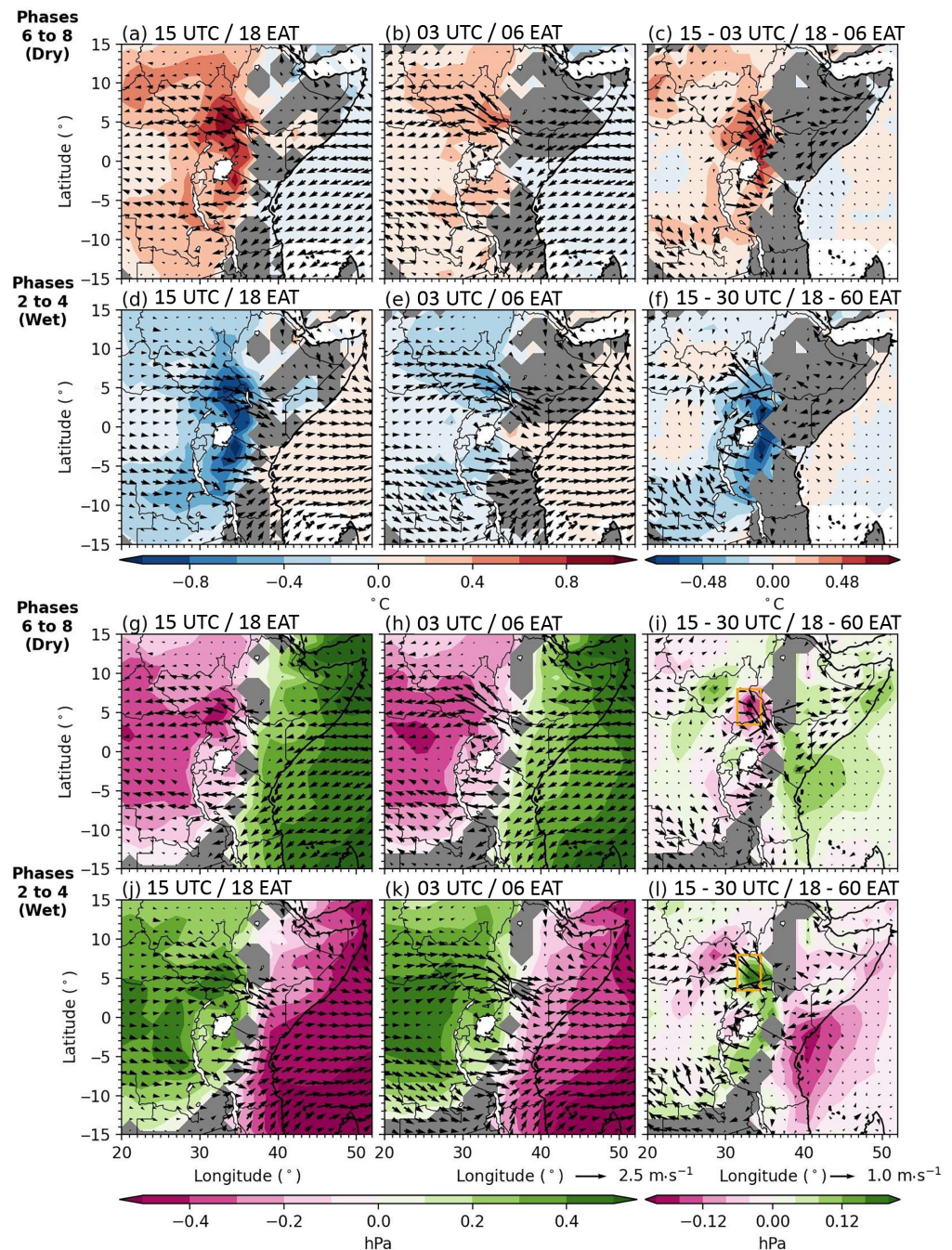
boundary layer and leads to a decreased geopotential height (Figure 4c,d) and shallow daytime ascent (not shown). As in Figure 3, surface-driven low-level warming peaks during the daytime, consistent with the diurnal cycle of surface heating (Figure 4a,b). During dry MJO days, the strengthening of the Turkana jet is very clear (Figure 4e,f), particularly at 0300 UTC. This jet intensification occurs below 700 hPa in a location determined by local orography (Kinuthia, 1992). The overnight anomalous jet strengthening is consistent with surface-induced enhancements to the local pressure gradient. During the daytime, dry convective mixing throughout the boundary

layer limits jet strength. Once a stable nocturnal surface layer develops, though, the jet can accelerate in response to the pressure gradient across the Turkana channel, which during dry MJO days is locally enhanced by surface heating. Diurnal jet fluctuations impact anomalous vertical velocity with stronger ascent across the exit region of the Turkana jet during nocturnal hours (not shown). Diurnal variations in the channel-orientated wind also influence anomalous specific humidity across the exit region of the Turkana channel (Figure 4g,h). Dry boundary-layer conditions are observed during the daytime associated with dry surface conditions. Meanwhile, the intensification
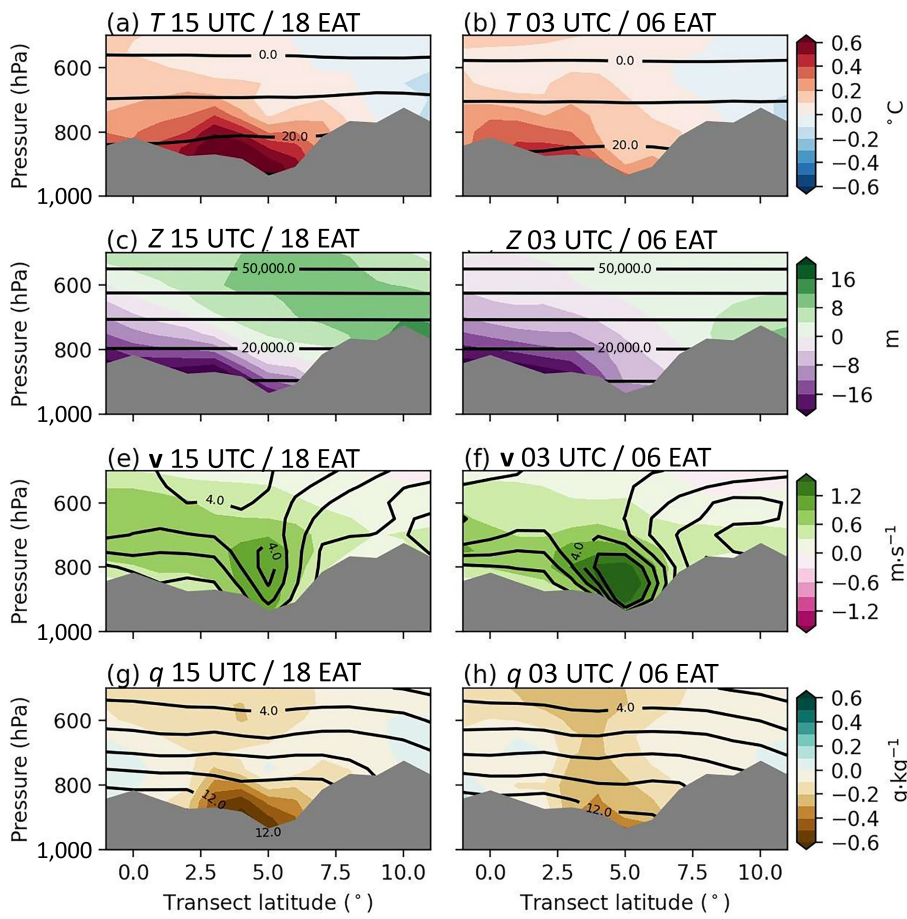
FIGURE 4 Vertical cross-section of average anomalies relative to the monthly climatology in (a, b) temperature (filled, °C), (c, d) geopotential height (filled, m), (e, f) channel-orientated wind speed (filled, m·s⁻¹), and (g, h) specific humidity (filled, g·kg⁻¹) during dry Madden–Julian oscillation days at (first column) 1500 UTC and (second column) 0300 UTC. Cross-sections are centred across the exit region of the Turkana jet and are perpendicular to the Turkana channel (domain shown in Figure 1a). Lined contours show the wet-season climatological values in intervals of 10°C, 10,000 m, 1.0 m·s⁻¹ and 2.0 g·kg⁻¹. Grey shading indicates the topography cross-section, which is based on the minimum surface pressure in the time series. [Colour figure can be viewed at wileyonlinelibrary.com]

of the Turkana jet after sunset weakens the negative anomaly of specific humidity due to moisture transport from low-lying coastal regions. The same processes, albeit of opposite sign, are also observed during wet MJO days, with surface cooling and moistening (Figure 2e,j) reducing daytime boundary-layer temperatures, increasing daytime low-level moisture, and weakening the nocturnal Turkana jet (Supporting Information Figure S3).

Through analysing diurnal variations in anomalous atmospheric conditions during dry and wet MJO days, it is evident that land–atmosphere feedbacks influence boundary-layer temperatures and may impact the Turkana jet (Figures 3 and 4). To further explore how the surface influences atmospheric conditions, we produce composite time series of dry and wet MJO events. For this analysis, an MJO event is defined as a period of at least 5 days when the MJO is in either a dry or wet MJO phase. After 5 days, we stop sampling the data if the MJO is no longer active in one of the appropriate phases. When including MJO events from both sampled seasons (MAM and OND), we composite across 130 dry events and 138 wet events. Focusing on dry events, Figure 5a illustrates the number of days in each MJO phase during our 15-day composite time series. Approximately 40%

of dry events initiate from an inactive MJO, whereas the remaining 60% commence from MJO phase 5, which is often described as a transitional phase across East Africa. The remaining panels in Figure 5 then show Hovmöller diagrams illustrating the surface and atmospheric evolution through a transect orientated along the Turkana channel (Figure 1b). We focus on the development of anomalous surface soil moisture, low-level atmospheric temperature, low-level atmospheric thickness, channel-orientated wind speed, and vertically integrated channel-orientated moisture flux. In this study we define low-level atmospheric thickness as the difference in geopotential height between 800 and 900 hPa. We also label regions with substantial surface gradients (Figure 1b), including the border of Sudan and South Sudan ("A"), the Turkana channel ("B"), and the Kenyan coastline ("C"). In addition, Figure 5 shows the mean diurnal cycle of anomalous atmospheric conditions between 32° and 37° longitude of days 2–6 of an MJO event. Figure 5b illustrates that surface drying strengthens around "B" between 33° and 38° longitude as a dry MJO event persists. These dry surface conditions drive daytime low-level atmospheric warming across the exit region of the Turkana jet (Figure 5c,d), and promote an increased atmospheric thickness that maximises

FIGURE 5 (a) The number of days in each Madden–Julian oscillation (MJO) phase in the dry MJO event composite. (b, c, e, g, i) Channel-orientated Hovmöller diagrams (with the cross-section orientated along the Turkana channel – domain shown in Figure 1b) of anomalies relative to the monthly climatology in (b) surface soil moisture ($m^3 \cdot m^{-3}$), (c) 850 hPa temperature (°C), (e) atmospheric thickness between 800 and 900 hPa (m), (g) 850 hPa channel-orientated wind speed ($m \cdot s^{-1}$), and (i) vertically integrated channel-orientated moisture flux ($kg \cdot m^{-1} \cdot s^{-1}$) during dry MJO events. Grey dashed horizontal lines, and associated labels, in Hovmöller diagrams highlight transect locations where there is a strong surface gradient parallel to the channel (Figure 1b). Mean diurnal cycles of average anomalous atmospheric conditions during days 2–6 and between 32.0° and 37.0° longitude (region denoted by black dashed rectangles in Hovmöller diagrams) are shown to the right of Hovmöller diagrams in (d), (f), (h), and (j). In these panels daytime hours (0300 to 1500 UTC) are highlighted with a light orange background. [Colour figure can be viewed at wileyonlinelibrary.com]
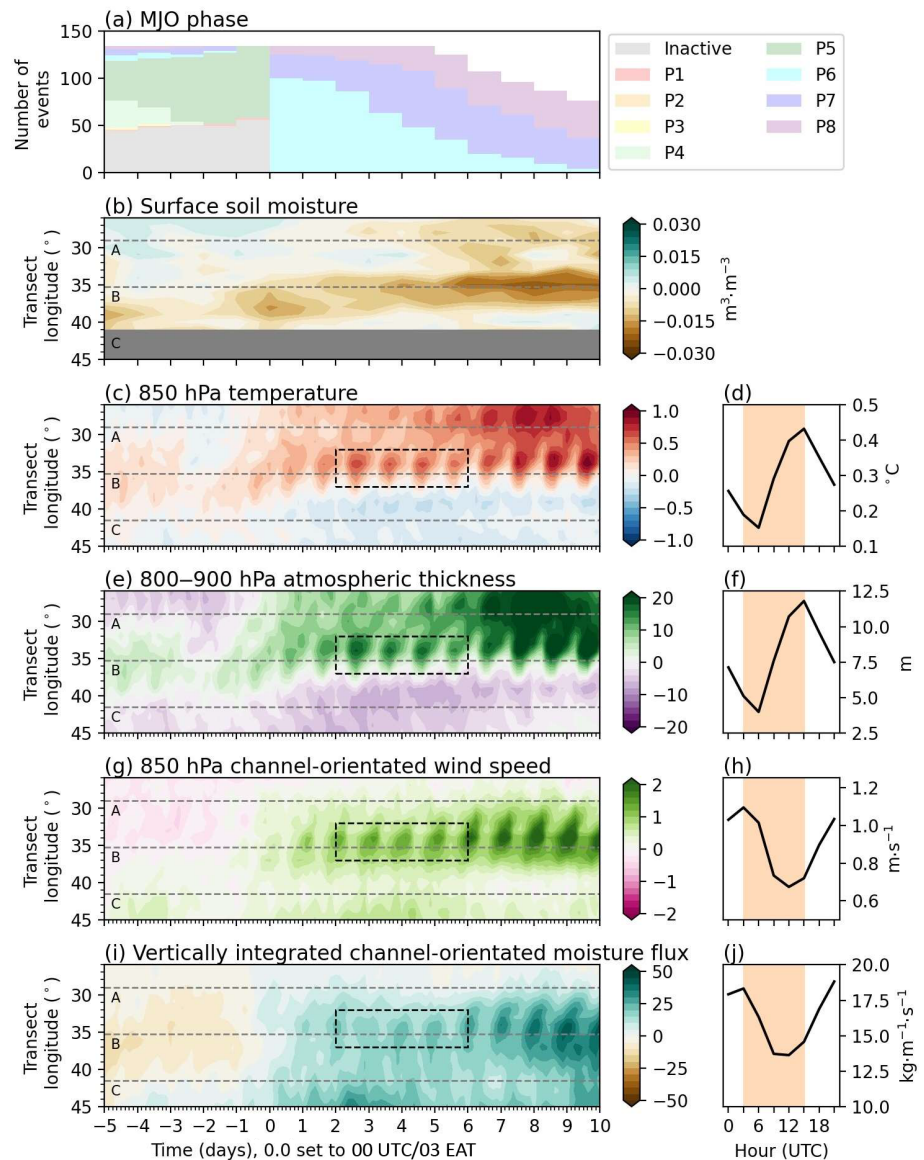
during the late afternoon (Figure 5e,f). The substantial along-channel gradient in anomalous low-level atmospheric temperature and thickness increases the pressure gradient between southern South Sudan and the Kenyan lowlands, which promotes a stronger Turkana jet (Figure 5g) and increases moisture transport through the Turkana channel (Figure 5i). A strengthened Turkana jet also promotes anomalous ascent in the exit region of the Turkana channel (not shown). Comparing the diurnal cycle of anomalous temperatures across southern South Sudan (Figure 5d) with climatology (not shown) re-emphasises a surface atmospheric forcing. Anomalous temperatures during a dry MJO event continue to increase during the late afternoon (1200 to 1500 UTC; Figure 5d) due to enhanced surface sensible heat fluxes, reducing the rate at which the atmosphere typically cools. The diurnal cycle of dynamical atmospheric conditions, including

channel-orientated wind speed and moisture flux, also indicates a surface-driven forcing, as anomalous conditions maximise during nocturnal hours when frictional forces induced by surface turbulent fluxes are weak. Similar processes are also observed during wet MJO events, where surface and low-level atmospheric cooling around "B" decreases the channel-orientated pressure gradient, weakens the Turkana jet, and reduces the moisture transport through the Turkana channel (Supporting Information Figure S4). In summary, the composite evolution presented here indicates that MJO-induced large-scale surface drying across the exit region of the Turkana jet increases the along-channel pressure gradient and thereby intensifies the Turkana jet.

Given the influence of continental-scale pressure anomalies on the Turkana jet (Fig. 3g-l; Finney *et al.*, 2020b) and uncertainties in surface flux forcing, it
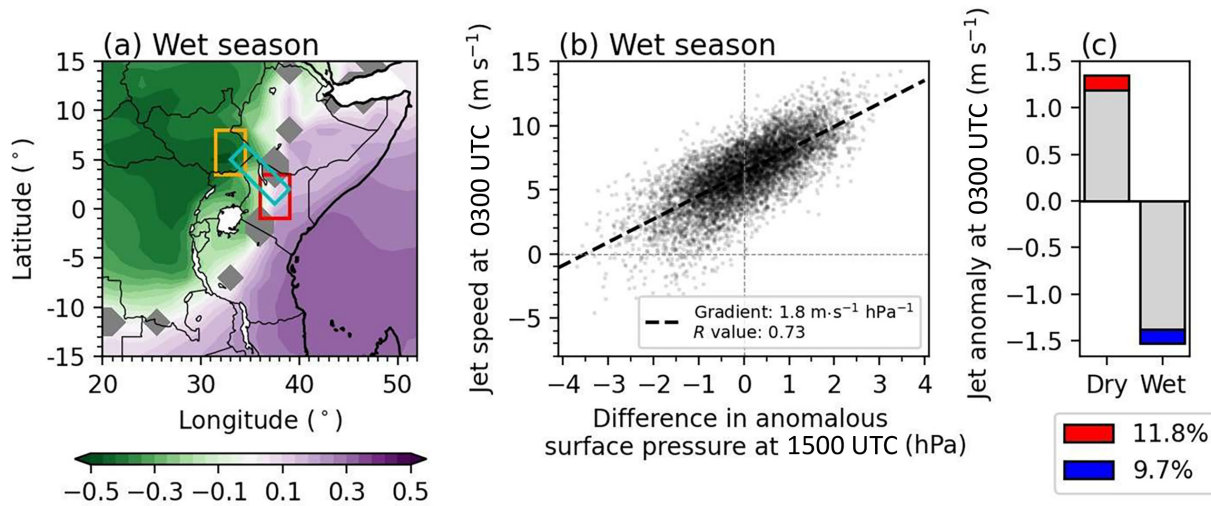
FIGURE 6 (a) Correlation coefficients between daily wet-season values of surface pressure at 1500 UTC and the Turkana jet speed at the following 0300 UTC. The cyan rectangle – corner points of (5.0° N, 33.0° E), (6.5° N, 34.5° E), (2.0° N, 39.0° E), (0.5° N, 37.5° E) from northwestern corner then following round in a clockwise direction – denotes the region used to calculate the average jet speed, whereas red (−1.0 to 3.5° N, 36–39° E) and orange (3.5–8.0° N, 31.5–34.5° E) rectangles highlight entrance and exit regions of the Turkana jet respectively. Correlation coefficients are only shown if the correlation between surface pressure and jet speed is significant at the 95% confidence level; grey shading denotes insignificant regions. (b) Scatter plot of wet-season daily values of the local anomalous surface pressure difference (hPa) at 1500 UTC and the Turkana jet speed (m·s^{-1}) at the following 0300 UTC. The local pressure difference is calculated by subtracting the anomalous surface pressure at the jet exit (orange square) from the anomaly at the jet entrance (red square). (c) The mean anomalous jet speed (m·s^{-1}) at 0300 UTC during dry and wet MJO days. Red and blue shading denote the proportion of jet speed attributable to daytime surface pressure variations across the exit region of the Turkana channel during dry and wet MJO days respectively. The legend shows the percentage of the anomalous jet speed attributable to surface forcing. [Colour figure can be viewed at wileyonlinelibrary.com]

is challenging to isolate the effect of anomalous surface fluxes on the nocturnal jet. Here, we exploit the diurnal cycle of surface forcing to estimate the impact of surface heating on the jet speed. Figure 6a shows correlation coefficients between wet-season daily data of late afternoon (1500 UTC) surface pressure and nocturnal (0300 UTC) Turkana jet speed. The cyan rectangle in Figure 6a – corner points of (5.0° N, 33.0° E), (6.5° N, 34.5° E), (2.0° N, 39.0° E), (0.5° N, 37.5° E) from northwestern corner then following round in a clockwise direction – highlights the region used to calculate the average jet speed from channel-orientated wind speed at 850 hPa. As expected, the nocturnal jet speed is correlated with continental-scale pressure differences from the preceding day. For example, increased surface pressure across the western Indian Ocean is associated with a stronger Turkana jet. Alongside a continental-scale spatial structure in correlations between surface pressure and jet speed, we observe a local maximum in the correlation coefficient across the southeast of South Sudan. As this region is co-located with large MJO-induced surface temperature anomalies (Figure 2g,j), it supports the hypothesis that MJO-driven surface-induced pressure changes influence the Turkana jet speed. Figure 6b illustrates the sensitivity of the nocturnal jet speed (0300 UTC) to the preceding afternoon

(1500 UTC) anomalous surface pressure difference across the Turkana channel using data from all wet-season days. For Figure 6b, the entrance and exit regions of the Turkana channel are denoted by red (−1.0 to 3.5° N, 36–39° E) and orange (3.5–8.0° E) rectangles respectively in Figure 6a. According to ERA5, the mean surface pressure in the exit region of the Turkana channel drops by 0.09 hPa during daytime hours on dry MJO days (Figure 3i). This enhances the pressure difference across the channel and, according to the linear regression in Figure 6b, intensifies the nocturnal jet by 0.16 m·s^{-1}. Given that the average nocturnal jet speed anomaly during a dry MJO day is 1.35 m·s^{-1}, and assuming anomalous daytime surface pressure fluctuations are predominantly controlled by surface flux anomalies, this indicates that surface-driven daytime pressure variations control approximately 11.8% of MJO-associated jet variability (Figure 6c). During wet MJO days, on the other hand, anomalous surface fluxes can be attributed to approximately 9.7% of the reduced jet speed. As shown in Figure 5i, nocturnal jet variations influence the amount of moisture transported through the Turkana channel. Correlating the nocturnal moisture flux through the Turkana channel with daytime pressure changes indicates that, on average, approximately 10% and 8% of the anomalous

moisture flux during a dry and wet MJO day respectively can be attributed to surface-driven jet speed variations (not shown).

In summary, whereas variability of the Turkana jet is primarily controlled by continental-scale pressure differences to the west and east of the East African Highlands (Finney *et al.*, 2020b), we highlight that surface flux variations amplify anomalies in jet speed and contribute an important local forcing. On each day during a dry MJO event, we estimate that surface-driven enhanced boundary-layer temperatures across the exit region of the Turkana channel are responsible for approximately 11.8% of the jet speed anomaly. However, our estimate of the surface forcing on the Turkana jet only considers localised daytime pressure changes, whereas heat anomalies will build up over multiple days during an MJO event. Given the predominantly easterly flow and substantial barrier presented by the mountains to the east, this accumulation of heat will lead to more sustained surface-induced pressure changes on the western side of the East African Highlands the longer an MJO event persists. Figure 5c,e, along with spatial maps of anomalous surface pressure and near-surface temperature (not shown), illustrates that temperature and pressure anomalies intensify to the west of the East African Highlands as an MJO event persists. Quantification of this surface effect requires either Lagrangian tracking of heat anomalies (Schumacher *et al.*, 2019) or numerical modelling experiments to fully understand the influence of surface-driven atmospheric heating on the Turkana jet. As well as this, and evident from Figure 5c, daytime temperature fluctuations are larger in the exit region of the Turkana channel as an MJO event persists, due to rapidly drying soils and progressively increasing sensible heat flux. This increased temperature perturbation results in larger daytime surface pressure fluctuations. For example, mean surface pressure decreases by 0.16 hPa during the daytime across the exit region of the Turkana channel during days 6–8 of a dry MJO event (not shown). This change in surface pressure can be attributed to a jet intensification of $0.29\,\mathrm{m\cdot s^{-1}}$, which is approximately 80% greater than the surface-driven jet intensification during an average dry MJO day (Figure 6c).

3.3 | Response of the East African moisture budget to MJO-induced surface–atmosphere feedbacks

We have shown evidence that the spatial variation in the surface response to MJO-induced anomalous precipitation influences the intensity of the Turkana jet (Section 3.2). Given that the Turkana jet controls moisture transport

from low-lying regions of East Africa into Central Africa (Vizy and Cook, 2019; Munday *et al.*, 2021), we expect surface-induced Turkana jet intensity variations to affect precipitation characteristics across East Africa. To investigate this hypothesis in more detail, we partition wet MJO events by surface soil moisture conditions before the MJO event itself. As moisture-induced surface turbulent flux anomalies across the exit region of the Turkana jet partly control the jet intensity, we expect a stronger jet if the surface is dry before a wet MJO event.

To partition wet MJO events by anomalous surface soil moisture across the exit region of the Turkana jet, we calculate the regional-mean surface soil moisture anomaly in southeast South Sudan (4–8° N, 31–35° E; region denoted by green squares in Figure 7a–c) during the five days preceding an MJO event. Similar to previous analysis, a wet MJO event is defined as a period of at least five days when the MJO is active in phases 2–4. However, an MJO event is only retained if at least three of the preceding five days have valid soil moisture observations across at least 20% of the South Sudan region. Using 5-day averages of anomalous surface soil moisture, we then partition wet MJO events in half, with subsets containing relatively dry or wet initial surface conditions across the exit region of the Turkana jet. Figure 7a,b shows the average anomalous 1200 UTC near-surface air temperature and 0000 UTC 850 hPa horizontal wind in the 5 days preceding a wet MJO event in each subset. We also show the differences between subsets in Figure 7c. Focusing on composite-mean atmospheric conditions before a wet MJO event, a dry or wet surface across the exit region of the Turkana jet is associated with anomalous easterlies or westerlies respectively across equatorial East Africa (Figure 7a,b). Anomalous easterlies are typically associated with drier conditions across continental regions of East Africa, as anomalous easterlies limit moisture transport from the Congolese rainforest (Finney *et al.*, 2020b). We also observe the largest near-surface temperature anomalies across the exit region of the Turkana jet due to anomalous surface soil moisture feeding back onto daytime atmospheric temperatures (Figure 7a–c).

We now consider precipitation and wind differences between our two samples during the wet MJO event itself (Figure 7d–f). We observe significant precipitation differences between the two samples across a wide area of East Africa, extending from central Tanzania up to northern Somalia. Alongside this, there are significant differences in the large-scale flow across the region. This suggests that our two samples are capturing differences in synoptic conditions well beyond any localised effects around the Turkana channel. Having said that, we also observe a significantly stronger Turkana jet when sampling drier antecedent soil conditions in
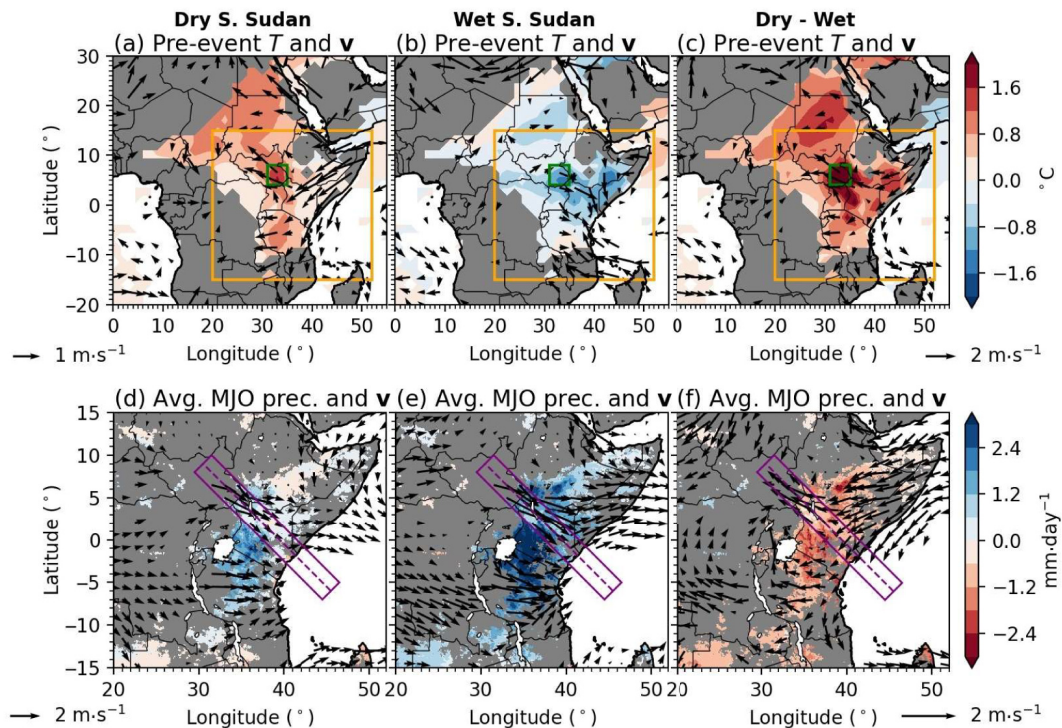
FIGURE 7 Average anomalies relative to a monthly climatology in (a–c) 1500 UTC near-surface air temperature (filled, °C) and 0300 UTC 850 hPa horizontal wind (vectors, m·s⁻¹) in the 5 days preceding wet Madden–Julian oscillation (MJO) events, and (d–f) daily accumulated precipitation (filled, mm· day⁻¹) and 0300 UTC 850 hPa horizontal wind (vectors, m·s⁻¹) during wet MJO events in each sample. Anomalies are shown for events that have been preceded by relatively (a, d) dry or (b, e) wet soils across the exit region of the Turkana jet. Panels (c) and (f) show the differences between the two subsets. Anomalies are only shown if there is a significant difference between the two subsets at the 95% confidence level. Wind vectors are displayed if the wind speed is significantly different in either a meridional or zonal direction. In panels (a)–(c), a green rectangle denotes the region used to compute the pre-MJO event anomalous surface soil moisture (4–8° N, 31–35° E), whereas an orange rectangle denotes the domain shown in panels (d)–(f). Purple transects in panels (d)–(f) show the domain used for averaging atmospheric conditions in Figure 8 [Colour figure can be viewed at wileyonlinelibrary.com]

South Sudan (Figure 7f). This localised difference in atmospheric conditions agrees with our proposed land feedback mechanism, albeit superimposed on larger scale circulation features of unknown origin. We also find reduced rainfall in the entrance region of the Turkana channel in the sample with drier antecedent soil conditions and a stronger jet. This link between surface-induced Turkana jet variations with East African precipitation is consistent with Munday *et al.* (2021), who showed a reduction in monthly accumulated April precipitation across the East African Highlands, southern Ethiopia, and southern Somalia, when the Turkana jet is relatively strong. It also agrees with Vizy and Cook (2019) and King *et al.* (2021), who illustrate a correlation between the Turkana jet speed and precipitation across equatorial East Africa. However, our samples differ in the large-scale circulation that gives rise to the initial soil moisture conditions (Figure 7a–c), and these differences may persist and influence the low-level flow in subsequent days across the wider region (Figure 7d–f). From our diagnostic approach, it is difficult to disentangle the

effects of local land feedbacks from larger scale processes. Modelling experiments are required to isolate the influence of surface-induced near-surface temperature variations across the exit region of the Turkana jet on East African precipitation.

We conclude our analysis by considering differences in the atmospheric water budget between each subset of MJO events, focusing on a region where we expect the Turkana jet to play a leading role (purple transect in Figure 7d–f). Figure 8a,b shows the average diurnal cycle of GPM IMERG three-hourly precipitation accumulations during wet MJO events that are preceded by dry and wet soils. Owing to the time span of available IMERG subdaily precipitation accumulations (Table 1), we only analyse wet MJO events between 2000 and 2020. Similar to Figure 5, we denote longitudes with substantial surface gradients (Figure 1b), with "B" and "C" indicating strong gradients across the Turkana channel and at the Kenyan coastline respectively. The diurnal cycles of precipitation show that afternoon (0900–1500 UTC/1200–1800 EAT) coastal convection is more intense and propagates further

FIGURE 8 Average diurnal cycle in (a–c) GPM IMERG precipitation (mm·hr^{-1}), and the (d–f) mean anomalous GPM IMERG precipitation (mm·hr^{-1}, blue bars) and ERA5 vertically integrated moisture flux convergence (mm·hr^{-1}, lined) between 36.5° E and 42.5° E. Average values are shown for wet MJO events that are preceded by (a,d) dry or (b,e) wet soils across the exit region of the Turkana jet (4–8° N, 31–35° E; region denoted by green squares in Figure 7a,c). Panels (c) and (f) show differences between the two subsets. Hovmöller diagrans in (a)–(c) are orientated along the Turkana channel with the domain shown in Figure 7d–f. In (a)–(c), rainfall totals are only shown if the difference between subsets is significant at a 95% confidence level. In (d)–(f), significance at a 95% confidence level is denoted by hatching or filled scatter points [Colour figure can be viewed at wileyonlinelibrary.com]
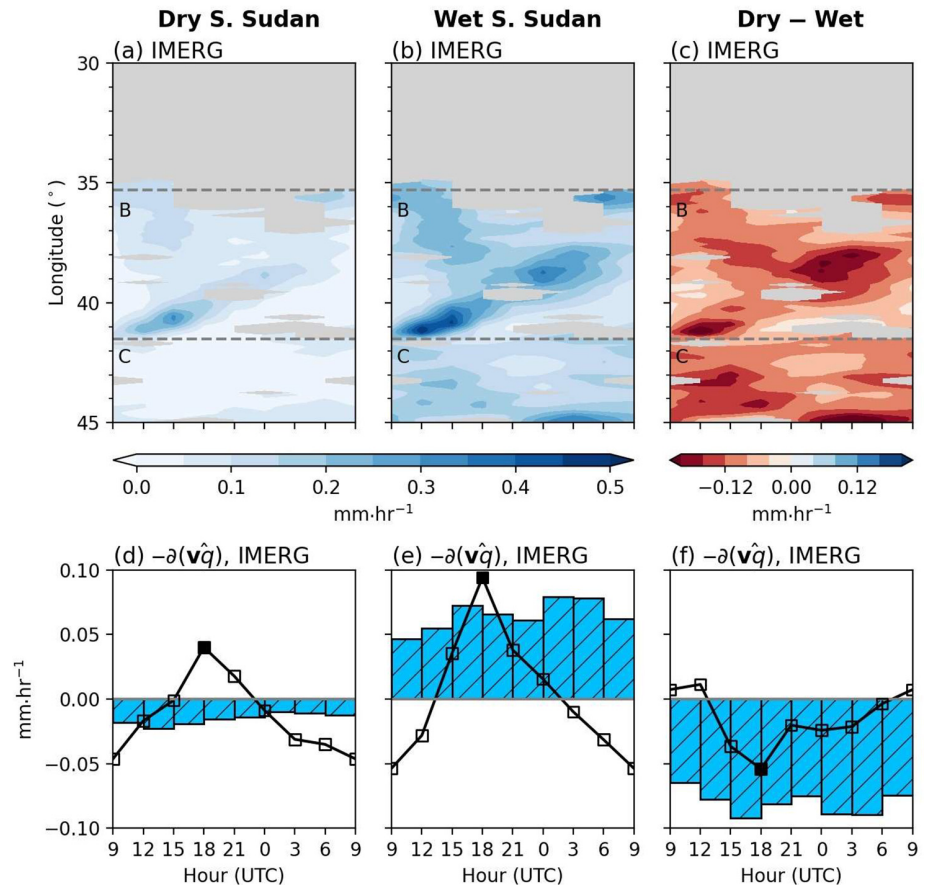
inland in the wet soil sample (Figure 8a–c). To understand the atmospheric drivers responsible for enhanced initiation and propagation of coastal convection, we analysed the diurnal cycle of the average anomalous vertically integrated moisture flux convergence and precipitation between the Turkana channel and coastline of Kenya (36.5–42.5° E along the transect). Figure 8d–f shows the diurnal cycle of anomalous vertically integrated moisture flux convergence and precipitation between these two locations. We find that there is enhanced moisture convergence during the evening (1500–2100 UTC/1800–0000 EAT) in both wet MJO phase samples compared with climatology. However, the wet soil sample shows consistently stronger and more prolonged moisture convergence throughout the night. This is expected to contribute to the extended lifetime of afternoon coastal convection as it propagates inland. In this way, soil moisture on the continental side of the Turkana channel may affect rainfall across a larger region of East Africa. However, we note that differences in moisture convergence in the ERA5 reanalysis are not large enough to balance the precipitation differences observed in the IMERG dataset. This is perhaps unsurprising given that ERA5 underestimates the true strength of the Turkana jet (Munday et al., 2022).

4 | DISCUSSION

This study shows that the considerable duration and intensity of MJO-induced precipitation variability promotes a land–atmosphere feedback across semi-arid regions of East Africa. Though previous studies have shown the importance of tropical intraseasonal land–atmosphere feedbacks in West Africa, India, and South America (Taylor, 2008; Saha et al., 2012; Chug and Dominguez, 2019; Talib et al., 2022), this is the first study to highlight such feedbacks across East Africa. Even though East African rainfall is influenced by multiple atmospheric drivers (Nicholson, 2017), and the land surface is orographically complex with a variety of biomes (Kinuthia and Asnani, 1982), we observe a consistent surface response to MJO-induced rainfall variability. In agreement with previous studies showing a sensitivity of surface fluxes to precipitation variability (Gallego-Elvira et al., 2016; Feldman et al., 2019), MJO-induced changes in surface soil moisture leads to a strong surface turbulent flux response across highland regions of southwest Kenya and northern Uganda and low-lying regions of South Sudan. The spatial variation in the surface flux response to MJO-induced anomalous precipitation affects the intensity of the Turkana jet.
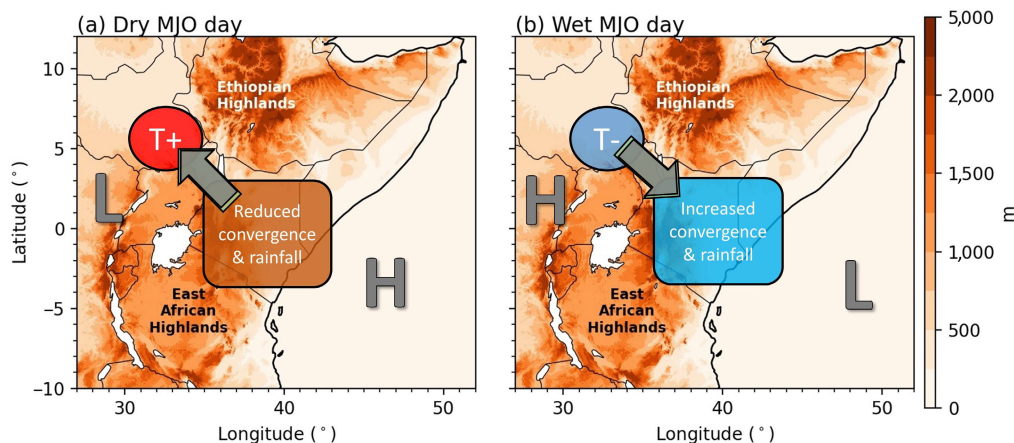
FIGURE 9 Schematic illustrating changes in low-tropospheric temperatures (circles), anomalous average jet wind speeds (green) with and (grey) without average surface-induced forcing over a single day (arrows), and fluctuations in moisture convergence and rainfall (ovals) across Kenya during (a) a dry and (b) a wet Madden–Julian oscillation (MJO) day. Large-scale surface pressure anomalies are denoted by letters "H" and "L" for high and low pressure respectively. The schematic background is the surface orography (m). Though we are only able to highlight the influence of the surface over the course of a single day, we expect that the accumulation of heat during multiple days to amplify jet anomalies further [Colour figure can be viewed at wileyonlinelibrary.com]

We conclude that whereas anomalous jet speeds are primarily controlled by continental-scale pressure anomalies (Finney *et al.*, 2020b), surface-induced pressure fluctuations across the exit region of the Turkana channel over the course of a single day are responsible for approximately 12% of the anomalous jet speed during a dry MJO event. The surface response to MJO-driven rainfall fluctuations enhances circulation anomalies associated with the MJO. We also expect that the accumulation of heat to the west of the East African Highlands over the course of an MJO event further amplifies the surface influence on the Turkana jet speed. Furthermore, in this work we propose that surface-driven Turkana jet variations affect the moisture budget on the coastal side of the East African and Ethiopian Highlands. In contrast to other tropical intraseasonal land–atmosphere feedback studies that focus on the local atmospheric response (Taylor, 2008; Saha *et al.*, 2012; Chug and Dominguez, 2019; Talib *et al.*, 2022), the control of surface soil moisture on the Turkana jet intensity and continental-scale moisture transport affects non-local atmospheric conditions. However, modelling experiments are required to fully quantify the effect of surface-driven atmospheric warming.

Alongside highlighting intraseasonal surface-driven Turkana jet variations, we argue that the Turkana jet influences precipitation characteristics across Kenya. Figure 9 is a schematic summarising surface-driven changes in atmospheric conditions during dry and wet MJO days in addition to circulation anomalies induced by large-scale pressure anomalies. Using wet MJO days as an example (Figure 9b), a surface-driven decreased

low-tropospheric temperature gradient across the Turkana channel, driven by reduced surface sensible heat fluxes in the exit region of the Turkana jet, decreases the along-channel pressure gradient, weakens the Turkana jet, and enables coastal convection to propagate further inland due to increased moisture convergence. This mechanism is consistent with Camberlin *et al.* (2019), who show a strong MJO-driven modulation of the diurnal cycle of rainfall in inland regions of Kenya, and amplifies anomalous atmospheric conditions associated with the MJO (Pohl and Camberlin, 2006a; Berhane and Zaitchik, 2014; Finney *et al.*, 2020b). Variations in rainfall driven by differences in the Turkana jet intensity and sea-breeze circulation are unlikely to be resolved in coarse-resolution general circulation models (GCMs). This is indicated by Finney *et al.* (2020a), who show that the inland propagation of coastal convection is stronger in high-resolution, explicit-convection simulations compared with a model set-up with parametrised convection and a coarser resolution. Though Finney *et al.* (2020a) argue that using parametrised convection does not fully represent a realistic rainfall response to sea-breeze circulations, we propose that the improved rainfall propagation in explicit-convection simulations may be partly associated with a weaker Turkana jet and increased low-level moisture convergence (Misiani *et al.*, 2020; Finney *et al.*, 2020a). Whereas previous work has studied model differences in the representation of the Turkana jet (King *et al.*, 2021), a thorough investigation into the observed and simulated relationship between the diurnal cycle of precipitation across equatorial East Africa and Turkana jet characteristics is yet to take place.

There are exceptional differences in the representation of the Turkana jet amongst the latest state-of-the-art GCMs (King *et al.*, 2021; Munday *et al.*, 2021; Oscar *et al.*, 2022). Given that the Turkana jet is more intense across narrower parts of the Turkana channel (Kinuthia, 1992), regional modelling experiments show a sensitivity of the jet to orography (Indeje *et al.*, 2001), and a more intense jet is simulated at finer model resolutions (Misiani *et al.*, 2020; Finney *et al.*, 2020a; Oscar *et al.*, 2022), it is frequently proposed that intermodel differences are caused by different horizontal resolutions and representations of orography (King *et al.*, 2021; Munday *et al.*, 2021). Meanwhile in this study, we highlight that variations in the Turkana jet intensity can be driven by channel-orientated gradients in LST. This is consistent with Hartman (2018), who argue that seasonal variations in jet strength are controlled by temperature differences across the Turkana channel. Given the observed impact of surface conditions on the Turkana jet in this study, and that the surface response to dry spells across East Africa varies amongst GCMs (Gallego-Elvira *et al.*, 2019), it may be the case that model differences in the representation of the Turkana jet (King *et al.*, 2021; Munday *et al.*, 2021) are partly influenced by simulated land-surface dynamics.

Through improving our understanding of intraseasonal land–atmosphere feedbacks across East Africa, we can support efforts to improve subseasonal to seasonal forecasts and aid the development of early warning systems of hydrometeorological extreme events. Whilst the phase of the MJO affects the likelihood of extreme rainfall (Finney *et al.*, 2020b), our study suggests that surface-induced Turkana jet variations may partly control the severity of an individual MJO event. As a result, even though current subseasonal forecast models utilise MJO-driven rainfall predictability (de Andrade *et al.*, 2021; Endris *et al.*, 2021; MacLeod *et al.*, 2021), additional skill may be obtained by an improved initialisation of the land surface or better evapotranspiration dynamics. The improved knowledge of subseasonal land–atmosphere feedbacks from this study not only encourages weather and climate model evaluation, but also motivates further investigation into the predictability gained from surface-induced Turkana jet variations across multiple time-scales.

5 | CONCLUSIONS

Through using multiple satellite-based datasets, we identify a surface soil moisture and turbulent flux response to MJO-induced precipitation variability across East Africa. The spatial variation in the surface response to MJO-induced anomalous precipitation influences the

Turkana jet intensity. For example, a dry MJO event promotes surface warming across the exit region of the Turkana channel, which strengthens the along-channel pressure gradient and intensifies the Turkana jet. Surface-driven pressure variations act as an additional forcing on jet characteristics, reinforcing the influence of large-scale pressure anomalies. Surface-driven jet variations also influence the moisture budget and precipitation characteristics across equatorial East Africa. For example, when the Turkana jet intensifies due to an enhanced surface-driven along-channel pressure gradient, moisture convergence and rainfall reduce across equatorial East Africa. This study is the first to highlight the importance of surface conditions on characteristics of the Turkana jet. As a result, it motivates idealised experiments to fully quantify surface-driven Turkana jet variations and their effect on precipitation across equatorial East Africa. It also encourages an investigation into whether subseasonal forecast models fully harness the predictability that can be obtained from the land surface in this sensitive region.

ORCID

Joshua Talib https://orcid.org/0000-0002-4183-1973

Christopher M. Taylor https://orcid.org/0000-0002-0120-3198

Bethan L. Harris https://orcid.org/0000-0002-0166-6256

Caroline M. Wainwright https://orcid.org/0000-0002-7311-7846

REFERENCES

Adler, R.F., Huffman, G.J., Chang, A., Ferraro, R., Xie, P.-P., Janowiak, J., Rudolf, B., Schneider, U., Curtis, S. and Bolvin, D. (2003) The version-2 global precipitation climatology project (GPCP) monthly precipitation analysis (1979–present). *Journal of Hydrometeorology*, 4, 1147–1167.

Aires, F., Weston, P., de Rosnay, P. and Fairbairn, D. (2021) Statistical approaches to assimilate ASCAT soil moisture information—I. Methodologies and first assessment. *Quarterly Journal of the Royal Meteorological Society*, 147, 1823–1852.

Annamalai, H. and Slingo, J. (2001) Active/break cycles: diagnosis of the intraseasonal variability of the Asian summer monsoon. *Climate Dynamics*, 18, 85–102.

Balsamo, G., Albergel, C., Beljaars, A., Boussetta, S., Brun, E., Cloke, H., Dee, D., Dutra, E., Muñoz-Sabater, J. and Pappenberger, F. (2015) ERA-interim/land: a global land surface reanalysis data set. *Hydrology and Earth System Sciences*, 19, 389–407.

Banta, R., Newsom, R., Lundquist, J., Pichugina, Y., Coulter, R. and Mahrt, L. (2002) Nocturnal low-level jet characteristics over Kansas during CASES-99. *Boundary-Layer Meteorology*, 105, 221–252.

Barton, E., Taylor, C., Klein, C., Harris, P. and Meng, X. (2021) Observed soil moisture impact on strong convection over mountainous Tibetan plateau. *Journal of Hydrometeorology*, 22, 561–572.

Berg, A., Lintner, B.R., Findell, K.L., Malyshev, S., Loikith, P.C. and Gentine, P. (2014) Impact of soil moisture–atmosphere interactions on surface temperature distribution. *Journal of Climate*, 27, 7976–7993.

Berhane, F. and Zaitchik, B. (2014) Modulation of daily precipitation over East Africa by the Madden–Julian oscillation. *Journal of Climate*, 27, 6016–6034.

Berhane, F., Zaitchik, B. and Badr, H.S. (2015) The Madden–Julian oscillation's influence on spring rainy season precipitation over equatorial West Africa. *Journal of Climate*, 28, 8653–8672.

Bhowmick, M. and Parker, D.J. (2018) Analytical solution to a thermodynamic model for the sensitivity of afternoon deep convective initiation to the surface bowen ratio. *Quarterly Journal of the Royal Meteorological Society*, 144, 2216–2229.

Blackadar, A.K. (1957) Boundary layer wind maxima and their significance for the growth of nocturnal inversions. *Bulletin of the American Meteorological Society*, 38, 283–290.

Bonner, W.D. (1968) Climatology of the low level jet. *Monthly Weather Review*, 96, 833–850.

Burrows, D.A., Ferguson, C.R., Campbell, M.A., Xia, G. and Bosart, L.F. (2019) An objective classification and analysis of upper-level coupling to the Great Plains low-level jet over the twentieth century. *Journal of Climate*, 32, 7127–7152.

Camberlin, P., Gitau, W., Kiladis, G., Bosire, E. and Pohl, B. (2019) Intraseasonal to interannual modulation of diurnal precipitation distribution over eastern Africa. *Journal of Geophysical Research: Atmospheres*, 124, 11863–11886.

Camberlin, P. and Philippon, N. (2002) The east African March–May rainy season: associated atmospheric dynamics and predictability over the 1968–97 period. *Journal of Climate*, 15, 1002–1019.

Campbell, M.A., Ferguson, C.R., Burrows, D.A., Beauharnois, M., Xia, G. and Bosart, L.F. (2019) Diurnal effects of regional soil moisture anomalies on the Great Plains low-level jet. *Monthly Weather Review*, 147, 4611–4631.

Chug, D. and Dominguez, F. (2019) Isolating the observed influence of vegetation variability on the climate of La Plata river basin. *Journal of Climate*, 32, 4473–4490.

Copernicus Climate Change Service (C3S). (2017) ERA5: Fifth Generation of ECMWF Atmospheric Reanalyses of the Global Climate. *Copernicus Climate Change Service Climate Data Store (CDS)*. URL: https://cds.climate.copernicus.eu/cdsapp#!/home.

de Andrade, F.M., Young, M.P., MacLeod, D., Hirons, L.C., Woolnough, S.J. and Black, E. (2021) Subseasonal precipitation prediction for Africa: forecast evaluation and sources of predictability. *Weather Forecasting*, 36, 265–284.

Dirmeyer, P.A. (2011) The terrestrial segment of soil moisture–climate coupling. *Geophysical Research Letters*, 38, 1–5.

Dirmeyer, P.A., Halder, S. and Bombardi, R. (2018) On the harvest of predictability from land states in a global forecast model. *Journal of Geophysical Research: Atmospheres*, 123, 13–111.

Dorigo, W., Wagner, W., Albergel, C., Albrecht, F., Balsamo, G., Brocca, L., Chung, D., Ertl, M., Forkel, M. and Gruber, A. (2017) ESA CCI soil moisture for improved earth system understanding: state-of-the art and future directions. *Remote Sensing of Environment*, 203, 185–215.

Du, Y., Zhang, Q., Chen, Y.-L., Zhao, Y. and Wang, X. (2014) Numerical simulations of spatial distributions and diurnal variations of low-level jets in China during early summer. *Journal of Climate*, 27, 5747–5767.

ECMWF. (2016) *Part II: Data Assimilation*. Cy41r2: IFS Documentation.

Endris, H.S., Hirons, L., Segele, Z.T., Gudoshava, M., Woolnough, S. and Artan, G.A. (2021) Evaluation of the skill of monthly precipitation forecasts from global prediction systems over the greater horn of Africa. *Weather Forecasting*, 36, 1275–1298.

Feldman, A.F., Short Gianotti, D.J., Trigo, I.F., Salvucci, G.D. and Entekhabi, D. (2019) Satellite-based assessment of land surface energy partitioning–soil moisture relationships and effects of confounding variables. *Water Resources Research*, 55, 10657–10677.

Ferguson, C.R., Agrawal, S., Beauharnois, M.C., Xia, G., Burrows, D.A. and Bosart, L.F. (2020) Assimilation of satellite-derived soil moisture for improved forecasts of the Great Plains low-level jet. *Monthly Weather Review*, 148, 4607–4627.

Ferranti, L., Slingo, J., Palmer, T. and Hoskins, B. (1999) The effect of land-surface feedbacks on the monsoon circulation. *Quarterly Journal of the Royal Meteorological Society*, 125, 1527–1550.

Finney, D.L., Marsham, J.H., Rowell, D.P., Kendon, E.J., Tucker, S.O., Stratton, R.A. and Jackson, L.S. (2020a) Effects of explicit convection on future projections of mesoscale circulations, rainfall, and rainfall extremes over eastern Africa. *Journal of Climate*, 33, 2701–2718.

Finney, D.L., Marsham, J.H., Walker, D.P., Birch, C.E., Woodhams, B.J., Jackson, L.S. and Hardy, S. (2020b) The effect of westerlies on east African rainfall and the associated role of tropical cyclones and the Madden–Julian oscillation. *Quarterly Journal of the Royal Meteorological Society*, 146, 647–664.

Folwell, S.S., Harris, P.P. and Taylor, C.M. (2016) Large-scale surface responses during European dry spells diagnosed from land surface temperature. *Journal of Hydrometeorology*, 17, 975–993.

Friedl, M. and Sulla-Menashe, D. (2015) MCD12Q1 MODIS/Terra+ aqua land cover type yearly L3 global 500m SIN grid V006 [data set]. *NASA EOSDIS Land Processes DAAC*, 10, 200.

Funk, C., Peterson, P., Landsfeld, M., Pedreros, D., Verdin, J., Shukla, S., Husak, G., Rowland, J., Harrison, L. and Hoell, A. (2015) The climate hazards infrared precipitation with stations—a new environmental record for monitoring extremes. *Scientific Data*, 2, 1–21.

Gadgil, S. and Asha, G. (1992) Intraseasonal variation of the summer monsoon I: observational aspects. *Journal of the Meteorological Society of Japan. Series II*, 70, 517–527.

Gallego-Elvira, B., Taylor, C.M., Harris, P.P. and Ghent, D. (2019) Evaluation of regional-scale soil moisture-surface flux dynamics in earth system models based on satellite observations of land surface temperature. *Geophysical Research Letters*, 46, 5480–5488.

Gallego-Elvira, B., Taylor, C.M., Harris, P.P., Ghent, D., Veal, K.L. and Folwell, S.S. (2016) Global observational diagnosis of soil moisture control on the land surface energy balance. *Geophysical Research Letters*, 43, 2623–2631.

Gelaro, R., McCarty, W., Suárez, M.J., Todling, R., Molod, A., Takacs, L., Randles, C.A., Darmenov, A., Bosilovich, M.G., Reichle, R., et al. (2017) The modern-era retrospective analysis for research and applications, version 2 (MERRA-2). *Journal of Climate*, 30, 5419–5454.

Gill, A.E. (1980) Some simple solutions for heat-induced tropical circulation. *Quarterly Journal of the Royal Meteorological Society*, 106, 447–462.

Giorgi, F. and Mearns, L.O. (2002) Calculation of average, uncertainty range, and reliability of regional climate changes from AOGCM simulations via the "reliability ensemble averaging" (REA) method. *Journal of Climate*, 15, 1141–1158.

Gruber, A., Dorigo, W.A., Crow, W. and Wagner, W. (2017) Triple collocation-based merging of satellite soil moisture retrievals. *IEEE Transactions on Geoscience and Remote Sensing*, 55, 6780–6792.

Gruber, A., Scanlon, T., van der Schalie, R., Wagner, W. and Dorigo, W. (2019) Evolution of the ESA CCI soil moisture climate data records and their underlying merging methodology. *Earth System Science Data*, 11, 717–739.

Guo, Z., Dirmeyer, P.A., Koster, R.D., Sud, Y., Bonan, G., Oleson, K.W., Chan, E., Verseghy, D., Cox, P., Gordon, C., et al. (2006) GLACE: the global land–atmosphere coupling experiment. Part II: analysis. *Journal of Hydrometeorology*, 7, 611–625.

Harris, B.L., Taylor, C.M., Weedon, G.P., Talib, J., Dorigo, W. and Van Der Schalie, R. (2022) Satellite-observed vegetation responses to intraseasonal precipitation variability. *Geophysical Research Letters*, 49, e2022GL099635.

Hartman, A.T. (2018) An analysis of the effects of temperatures and circulations on the strength of the low-level jet in the Turkana channel in East Africa. *Theoretical and Applied Climatology*, 132, 1003–1017.

Helfand, H.M. and Schubert, S.D. (1995) Climatology of the simulated Great Plains low-level jet and its contribution to the continental moisture budget of the United States. *Journal of Climate*, 8, 784–806.

Hersbach, H., Bell, B., Berrisford, P., Hirahara, S., Horányi, A., Muñoz-Sabater, J., Nicolas, J., Peubey, C., Radu, R. and Schepers, D. (2020) The ERA5 global reanalysis. *Quarterly Journal of the Royal Meteorological Society*, 146, 1999–2049.

Hersbach, H., Bell, W., Berrisford, P., Horányi, A.J.M.-S., Nicolas, J., Radu, R., Schepers, D., Simmons, A., Soci, C. and Dee, D. (2019) Global Reanalysis: Goodbye ERA-Interim, Hello ERA5. 17–24. URL: https://www.ecmwf.int/node/19027.

Hersbach, H., de Rosnay, P., Bell, B., Schepers, D., Simmons, A., Soci, C., Abdalla, S., Alonso-Balmaseda, M., Balsamo, G., Bechtold, P., Berrisford, P., Bidlot, J.-R., de Boisséson, E., Bonavita, M., Browne, P., Buizza, R., Dahlgren, P., Dee, D., Dragani, R., Diamantakis, M., Flemming, J., Forbes, R., Geer, A.J., Haiden, T., Hólm, E., Haimberger, L., Hogan, R., Horányi, A., Janiskova, M., Laloyaux, P., Lopez, P., Munoz-Sabater, J., Peubey, C., Radu, R., Richardson, D., Thépaut, J.-N., Vitart, F., Yang, X., Zsótér, E. and Zuo, H. (2018) Operational Global Reanalysis: Progress, Future Directions and Synergies with NWP. URL: https://www.ecmwf.int/node/18765.

Holton, J.R. (1967) The diurnal boundary layer wind oscillation above sloping terrain. *Tellus*, 19, 200–205.

Huffman, G., Stocker, E., Bolvin, D., Nelkin, E. and Jackson, T. (2019) GPM IMERG final precipitation L3 1 day 0.1 degree x 0.1 degree v06. In: Savtchenko, A. (Ed.) *Earth Sciences Data and Information Services Center (GES DISC)*. Greenbelt, MD, Goddard. https://doi.org/10.5067/GPM/IMERGDF/DAY/06.

Indeje, M., Semazzi, F.H., Xie, L. and Ogallo, L.J. (2001) Mechanistic model simulations of the east African climate using NCAR regional climate model: influence of large-scale orography on the Turkana low-level jet. *Journal of Climate*, 14, 2710–2724.

Kalnay, E., Kanamitsu, M., Kistler, R., Collins, W., Deaven, D., Gandin, L., Iredell, M., Saha, S., White, G. and Woollen, J. (1996) The NCEP/NCAR 40-year reanalysis project. *Bulletin of the American Meteorological Society*, 77, 437–472.

Kato, S., Rose, F.G., Rutan, D.A., Thorsen, T.J., Loeb, N.G., Doelling, D.R., Huang, X., Smith, W.L., Su, W. and Ham, S.-H. (2018) Surface irradiances of edition 4.0 clouds and the earth's radiant energy system (CERES) energy balanced and filled (EBAF) data product. *Journal of Climate*, 31, 4501–4527.

King, J.A., Engelstaedter, S., Washington, R. and Munday, C. (2021) Variability of the Turkana low-level jet in reanalysis and models: implications for rainfall. *Journal of Geophysical Research: Atmospheres*, 126, e2020JD034154.

Kinuthia, J. and Asnani, G. (1982) A newly found jet in North Kenya (Turkana channel). *Monthly Weather Review*, 110, 1722–1728.

Kinuthia, J.H. (1992) Horizontal and vertical structure of the Lake Turkana jet. *Journal of Applied Meteorology and Climatology*, 31, 1248–1274.

Klein, C. and Taylor, C.M. (2020) Dry soils can intensify mesoscale convective systems. *Proceedings of the National Academy of Sciences*, 117, 21132–21137.

Konings, A.G., Holtzman, N.M., Rao, K., Xu, L. and Saatchi, S.S. (2021) Interannual variations of vegetation optical depth are due to both water stress and biomass changes. *Geophysical Research Letters*, 48, e2021GL095267.

Koster, R., Mahanama, S., Yamada, T., Balsamo, G., Berg, A., Boisserie, M., Dirmeyer, P., Doblas-Reyes, F., Drewitt, G. and Gordon, C. (2011) The second phase of the global land–atmosphere coupling experiment: soil moisture contributions to subseasonal forecast skill. *Journal of Hydrometeorology*, 12, 805–822.

Koster, R., Schubert, S. and Suarez, M. (2009) Analyzing the concurrence of meteorological droughts and warm periods, with implications for the determination of evaporative regime. *Journal of Climate*, 22, 3331–3341.

Lavender, S.L. and Matthews, A.J. (2009) Response of the west African monsoon to the Madden–Julian oscillation. *Journal of Climate*, 22, 4097–4116.

Liebmann, B. and Smith, C.A. (1996) Description of a complete (interpolated) outgoing longwave radiation dataset. *Bulletin of the American Meteorological Society*, 77, 1275–1277.

Loeb, N.G., Manalo-Smith, N., Kato, S., Miller, W.F., Gupta, S.K., Minnis, P. and Wielicki, B.A. (2003) Angular distribution models for top-of-atmosphere radiative flux estimation from the clouds and the Earth's radiant energy system instrument on the tropical rainfall measuring mission satellite. Part I: methodology. *Journal of Applied Meteorology*, 42, 240–265.

Lu, J., Wang, G., Chen, T., Li, S., Hagan, D.F.T., Kattel, G., Peng, J., Jiang, T. and Su, B. (2021) A harmonized global land evaporation dataset from model-based products covering 1980–2017. *Earth System Science Data*, 13, 5879–5898.

MacLeod, D.A., Dankers, R., Graham, R., Guigma, K., Jenkins, L., Todd, M.C., Kiptum, A., Kilavi, M., Njogu, A. and Mwangi, E. (2021) Drivers and subseasonal predictability of heavy rainfall in equatorial east africa and relationship with flood risk. *Journal of Hydrometeorology*, 22, 887–903.

Madden, R.A. and Julian, P.R. (1994) Observations of the 40–50-day tropical oscillation—a review. *Monthly Weather Review*, 122, 814–837.

Matsuno, T. (1966) Quasi-geostrophic motions in the equatorial area. *Journal of the Meteorological Society of Japan. Series II*, 44, 25–43.

Meesters, A.G., De Jeu, R.A. and Owe, M. (2005) Analytical derivation of the vegetation optical depth from the microwave polarization difference index. *IEEE Geoscience and Remote Sensing Letters*, 2, 121–123.

Minnis, P., Sun-Mack, S., Chen, Y., Khaiyer, M.M., Yi, Y., Ayers, J.K., Brown, R.R., Dong, X., Gibson, S.C. and Heck, P.W. (2011) CERES edition-2 cloud property retrievals using TRMM VIRS and Terra and Aqua MODIS data—part II: examples of average results and comparisons with other data. *IEEE Transactions on Geoscience and Remote Sensing*, 49, 4401–4430.

Miralles, D., De Jeu, R., Gash, J., Holmes, T. and Dolman, A. (2011) Magnitude and variability of land evaporation and its components at the global scale. *Hydrology and Earth System Sciences*, 15, 967–981.

Miralles, D., Van Den Berg, M., Teuling, A. and De Jeu, R. (2012) Soil moisture-temperature coupling: a multiscale observational analysis. *Geophysical Research Letters*, 39, L21707.

Misiani, H.O., Finney, D.L., Segele, Z.T., Marsham, J.H., Tadege, A., Artan, G. and Atheru, Z. (2020) Circulation patterns associated with current and future rainfall over Ethiopia and South Sudan from a convection-permitting model. *Atmosphere*, 11, 1352.

Moesinger, L., Dorigo, W., de Jeu, R., van der Schalie, R., Scanlon, T., Teubner, I. and Forkel, M. (2020) The global long-term microwave vegetation optical depth climate archive (VODCA). *Earth System Science Data*, 12, 177–196.

Momen, M., Wood, J.D., Novick, K.A., Pangle, R., Pockman, W.T., McDowell, N.G. and Konings, A.G. (2017) Interacting effects of leaf water potential and biomass on vegetation optical depth. *Journal of Geophysical Research: Biogeosciences*, 122, 3031–3046.

Moron, V. and Robertson, A.W. (2021) Relationships between subseasonal-to-seasonal predictability and spatial scales in tropical rainfall. *International Journal of Climatology*, 41, 5596–5624.

Mpeta, E.J. and Jury, M.R. (2001) Intra-seasonal convective structure and evolution over tropical east Africa. *Climate Research*, 17, 83–92.

Munday, C., Engelstaedter, S., Ouma, G., Ogutu, G., Olago, D., Ong'ech, D., Lees, T., Wanguba, B., Nkatha, R. and Ogalo, C. (2022) Observations of the Turkana jet and the east African dry tropics: the RIFTJet field campaign. *Bulletin of the American Meteorological Society*, 103(8), E1828–E1842.

Munday, C., Savage, N., Jones, R.G. and Washington, R. (2023) Valley formation aridifies east Africa and elevates Congo basin rainfall. *Nature*, 615, 276–279.

Munday, C., Washington, R. and Hart, N. (2021) African low-level jets and their importance for water vapor transport and rainfall. *Geophysical Research Letters*, 48, e2020GL090999.

Muñoz Sabater, J. (2019) ERA5-Land hourly data from 1981 to present, Copernicus Climate Change Service (C3S) Climate Data Store (CDS).

Mutai, C.C. and Ward, M.N. (2000) East African rainfall and the tropical circulation/convection on intraseasonal to interannual timescales. *Journal of Climate*, 13, 3915–3939.

Nicholson, S. (2016) The Turkana low-level jet: mean climatology and association with regional aridity. *International Journal of Climatology*, 36, 2598–2614.

Nicholson, S.E. (2017) Climate and climatic variability of rainfall over eastern Africa. *Reviews of Geophysics*, 55, 590–635.

Oscar, L., Nzau, M.J., Ellen, D., Franklin, O., Rachel, J., Richard, W. and Tom, W. (2022) Characteristics of the turkana low-level jet stream and the associated rainfall in CMIP6 models. *Climate Dynamics*. https://doi.org/10.1007/s00382-022-06499-4.

Parish, T.R. and Oolman, L.D. (2010) On the role of sloping terrain in the forcing of the Great Plains low-level jet. *Journal of the Atmospheric Sciences*, 67, 2690–2699.

Parker, D., Burton, R., Diongue-Niang, A., Ellis, R., Felton, M., Taylor, C., Thorncroft, C., Bessemoulin, P. and Tompkins, A. (2005) The diurnal cycle of the west African monsoon circulation. *Quarterly Journal of the Royal Meteorological Society*, 131, 2839–2860.

Peng, J., Loew, A. and Crueger, T. (2017) The relationship between the Madden-Julian oscillation and the land surface soil moisture. *Remote Sensing of Environment*, 203, 226–239.

Pielke, R.A., Sr. (2001) Influence of the spatial distribution of vegetation and soils on the prediction of cumulus convective rainfall. *Reviews of Geophysics*, 39, 151–177.

Pohl, B. and Camberlin, P. (2006a) Influence of the Madden–Julian oscillation on east African rainfall. I: Intraseasonal variability and regional dependency. *Quarterly Journal of the Royal Meteorological Society*, 132, 2521–2539.

Pohl, B. and Camberlin, P. (2006b) Influence of the Madden–Julian oscillation on east African rainfall: II. March–May season extremes and interannual variability. *Quarterly Journal of the Royal Meteorological Society: A Journal of the Atmospheric Sciences, Applied Meteorology and Physical Oceanography*, 132, 2541–2558.

Rienecker, M.M., Suarez, M., Todling, R., Bacmeister, J., Takacs, L., Liu, H., Gu, W., Sienkiewicz, M., Koster, R. and Gelaro, R. (2008) The GEOS-5 data assimilation system. *Documentation of Versions*, 5.0. 1, 5.1. 0, and 5.2. 0.

Rodell, M., Houser, P., Jambor, U., Gottschalck, J., Mitchell, K., Meng, C.-J., Arsenault, K., Cosgrove, B., Radakovich, J. and Bosilovich, M. (2004) The global land data assimilation system. *Bulletin of the American Meteorological Society*, 85, 381–394.

Rodríguez-Fernández, N.J., Mialon, A., Mermoz, S., Bouvet, A., Richaume, P., Al Bitar, A., Al-Yaari, A., Brandt, M., Kaminski, T. and Le Toan, T. (2018) An evaluation of SMOS L-band vegetation optical depth (L-VOD) data sets: high sensitivity of L-VOD to above-ground biomass in Africa. *Biogeosciences*, 15, 4627–4645.

Saha, S.K., Halder, S., Suryachandra Rao, A. and Goswami, B. (2012) Modulation of ISOs by land-atmosphere feedback and contribution to the interannual variability of Indian summer monsoon. *Journal of Geophysical Research: Atmospheres*, 117, D13101.

Schumacher, D.L., Keune, J., Van Heerwaarden, C.C., Vilà-Guerau de Arellano, J., Teuling, A.J. and Miralles, D.G. (2019) Amplification of mega-heatwaves through heat torrents fuelled by upwind drought. *Nature Geoscience*, 12, 712–717.

Schwingshackl, C., Hirschi, M. and Seneviratne, S.I. (2017) Quantifying spatiotemporal variations of soil moisture control on surface energy balance and near-surface air temperature. *Journal of Climate*, 30, 7105–7124.

Sikka, D. and Gadgil, S. (1980) On the maximum cloud zone and the ITCZ over Indian longitudes during the southwest monsoon. *Monthly Weather Review*, 108, 1840–1853.

Soares, P.M., Careto, J.A., Cardoso, R.M., Goergen, K. and Trigo, R.M. (2019) Land-atmosphere coupling regimes in a future climate in Africa: from model evaluation to projections based on CORDEX-Africa. *Journal of Geophysical Research: Atmospheres*, 124, 11118–11142.

Sobrino, J. and Romaguera, M. (2004) Land surface temperature retrieval from MSG1-SEVIRI data. *Remote Sensing of Environment*, 92, 247–254.

Srinivasan, J., Gadgil, S. and Webster, P. (1993) Meridional propagation of large-scale monsoon convective zones. *Meteorology and Atmospheric Physics*, 52, 15–35.

Talib, J., Taylor, C.M., Klein, C., Harris, B.L., Anderson, S.R. and Semeena, V.S. (2022) The sensitivity of the west African monsoon circulation to intraseasonal soil moisture feedbacks. *Quarterly Journal of the Royal Meteorological Society*, 148, 1709–1730.

Taylor, C.M. (2008) Intraseasonal land–atmosphere coupling in the west African monsoon. *Journal of Climate*, 21, 6636–6648.

Taylor, C.M. (2015) Detecting soil moisture impacts on convective initiation in Europe. *Geophysical Research Letters*, 42, 4631–4638.

Taylor, C.M., de Jeu, R.A., Guichard, F., Harris, P.P. and Dorigo, W.A. (2012) Afternoon rain more likely over drier soils. *Nature*, 489, 423–426.

Taylor, C.M., Parker, D.J. and Harris, P.P. (2007) An observational case study of mesoscale atmospheric circulations induced by soil moisture. *Geophysical Research Letters*, 34. https://doi.org/10.1029/2007GL030572

Teuling, A., Seneviratne, S.I., Williams, C. and Troch, P.A. (2006) Observed timescales of evapotranspiration response to soil moisture. *Geophysical Research Letters*, 33. https://doi.org/10.1029/2006GL028178

Trigo, I.F., Monteiro, I.T., Olesen, F. and Kabsch, E. (2008) An assessment of remotely sensed land surface temperature. *Journal of Geophysical Research: Atmospheres*, 113. https://doi.org/10.1029/2008JD010035

Ulaby, F.T. (1982) Microwave remote sensing active and passive. *Rader Remote Sensing and Surface Scattering and Emission Theory*, 848–902. https://ntrs.nasa.gov/citations/19830032822

Unnikrishnan, C., Rajeevan, M. and Rao, S.V.B. (2017) A study on the role of land-atmosphere coupling on the south Asian monsoon climate variability using a regional climate model. *Theoretical and Applied Climatology*, 127, 949–964.

van den Hurk, B., Doblas-Reyes, F., Balsamo, G., Koster, R.D., Seneviratne, S.I. and Camargo, H. (2012) Soil moisture effects on seasonal temperature and precipitation forecast scores in Europe. *Climate Dynamics*, 38, 349–362.

van der Schalie, R., de Jeu, R.A., Kerr, Y.H., Wigneron, J.P., Rodríguez-Fernández, N.J., Al-Yaari, A., Parinussa, R.M., Mecklenburg, S. and Drusch, M. (2017) The merging of radiative transfer based surface soil moisture data from SMOS and AMSR-E. *Remote Sensing of Environment*, 189, 180–193.

van der Schalie, R., Preimesberger, W., Pasik, A., Scanlon, T. and Kidd, R. (2021) ESA climate change initiative plus soil moisture. Product user guide (PUG). URL: https://cds.climate.copernicus.eu/cdsapp#!/home.

Viste, E. and Sorteberg, A. (2013) Moisture transport into the Ethiopian highlands. *International Journal of Climatology*, 33, 249–263.

Vizy, E.K. and Cook, K.H. (2019) Observed relationship between the Turkana low-level jet and boreal summer convection. *Climate Dynamics*, 53, 4037–4058.

Wagner, W., Hahn, S., Kidd, R., Melzer, T., Bartalis, Z., Hasenauer, S., Figa-Saldana, J., De Rosnay, P., Jann, A. and Schneider, S. (2013) The ASCAT soil moisture product: a review of its specifications, validation results, and emerging applications. *Meteorologische Zeitschrift*, 22, 1–29.

Wan, Z. and Hook, G.H.S. (2015) Mod11a1 modis/terra land surface temperature/emissivity daily l3 global 1km sin grid v006. distributed by NASA EOSDIS Land Processes DAAC. URL: https://doi.org/10.5067/MODIS/MOD11A1.006.

Webster, P.J. (1983) Mechanisms of monsoon low-frequency variability: surface hydrological effects. *Journal of Atmospheric Sciences*, 40, 2110–2124.

Wheeler, M.C. and Hendon, H.H. (2004) An all-season real-time multivariate MJO index: development of an index for monitoring and prediction. *Monthly Weather Review*, 132, 1917–1932.

Yang, W., Seager, R., Cane, M.A. and Lyon, B. (2015) The annual cycle of east african precipitation. *Journal of Climate*, 28, 2385–2404.

SUPPORTING INFORMATION

Additional supporting information can be found online in the Supporting Information section at the end of this article.